Another baryon miracle? Testing solutions to the 'missing dwarfs' problem

Monthly Notices
of the
ROYAL ASTRONOMICAL SOCIETY

MNRAS **475,** 4825–4840 (2018)
Advance Access publication 2018 January 17

doi:10.1093/mnras/sty146

Another baryon miracle? Testing solutions to the 'missing dwarfs' problem

Sebastian Trujillo-Gomez,[1,2]★ Aurel Schneider,[3] Emmanouil Papastergis,[4] Darren S. Reed[1,2,5] and George Lake[1,2]

[1]*Center for Theoretical Astrophysics and Cosmology, University of Zurich, CH-8057 Zurich, Switzerland*
[2]*Institute for Computational Science, University of Zurich, CH-8057 Zurich, Switzerland*
[3]*Institute for Astronomy, Department of Physics, ETH Zurich, Wolfgang-Pauli-Strasse 27, CH-8093 Zurich, Switzerland*
[4]*Kapteyn Astronomical Institute, University of Groningen, Landleven 12, NL-9747 AD Groningen, the Netherlands*
[5]*S3IT, University of Zurich, CH-8057 Zurich, Switzerland*

Accepted 2018 January 4. Received 2018 January 4; in original form 2017 January 17

ABSTRACT

The dearth of dwarf galaxies in the local Universe is hard to reconcile with the large number of low-mass haloes expected within the concordance Λ cold dark matter (ΛCDM) paradigm. In this paper, we perform a systematic evaluation of the uncertainties affecting the measurement of dark matter halo abundance using galaxy kinematics. Using a large sample of dwarf galaxies with spatially resolved kinematics, we derive a correction to obtain the abundance of galaxies as a function of maximum circular velocity – a direct probe of halo mass – from the line-of-sight velocity function in the Local Volume. This method provides a direct means of comparing the predictions of theoretical models and simulations (including non-standard cosmologies and novel galaxy formation physics) to the observational constraints. The new 'galactic $V_{\rm max}$' function is steeper than the line-of-sight velocity function but still shallower than the theoretical CDM expectation, implying that unaccounted baryonic physics may be necessary to reduce the predicted abundance of galaxies. Using the galactic $V_{\rm max}$ function, we investigate the theoretical effects of feedback-powered outflows and photoevaporation of gas due to reionization. At the 3σ confidence level, we find that feedback and reionization are not effective enough to reconcile the disagreement. In the case of maximum baryonic effects, the theoretical prediction still deviates significantly from the observations for $V_{\rm max} < 60$ km s^{-1}. CDM predicts at least 1.8 times more galaxies with $V_{\rm max} = 50$ km s^{-1} and 2.5 times more than observed at 30 km s^{-1}. Recent hydrodynamic simulations seem to resolve the discrepancy but disagree with the properties of observed galaxies with spatially resolved kinematics. This abundance problem might point to the need to modify cosmological predictions at small scales.

Key words: galaxies: dwarf – galaxies: formation – galaxies: haloes – galaxies: kinematics and dynamics – dark matter – cosmology: theory.

1 INTRODUCTION

Dwarf galaxies provide a wealth of information on the formation of the smallest bound structures in the Universe. They are also excellent laboratories for understanding the physics that gives rise to galaxies. However, the cosmological properties of dark matter (DM) haloes and the observed properties of the galaxies they host can be challenging to disentangle.

A direct way to test the predictions of the cold dark matter (CDM) model at small scales is to measure the observed abundance of DM haloes. However, since DM is not directly observable, we are left with observable galaxies (and perhaps galaxy voids) as the 'peaks of the icebergs' from which to infer the abundance of their host DM haloes. This leads to several complications, including the fact that physical processes such as supernova energy release and photoheating due to reionization may have a strong effect on the fraction of haloes that host galaxies, as well as on the detectability of these objects.

In the last two decades, the CDM model has been confronted with several 'small-scale' problems. First, the 'missing satellites' refers to the underabundance of Milky Way (MW) satellite galaxies when compared to the predictions of gravity-only cosmological simulations (Klypin et al. 1999; Moore et al. 1999). Photoevaporation of

★ E-mail: strujill@gmail.com

gas from the lowest mass haloes was presumed to be responsible for the dearth of observed satellite galaxies, although the scale and impact of this process is still under debate (Gnedin 2000; Somerville 2002; Hoeft et al. 2006; Nagashima & Okamoto 2006; Okamoto, Gao & Theuns 2008).

More recently, new measurements of the central mass distributions of these galactic satellites allowed the CDM theory to be tested in more detail. It was found that the central velocity dispersions of the MW dwarf spheroidals are too low to host the most massive DM subhaloes predicted by *N*-body simulations. The so-called too big to fail problem is more serious and difficult to solve than the missing satellites because it relates the abundance to the structure of DM haloes using densities instead of luminosities (Boylan-Kolchin, Bullock & Kaplinghat 2011). At a given mass or circular velocity, the cosmic abundance of haloes is predicted by cosmology to exquisite precision (e.g. Springel et al. 2005; Diemand, Kuhlen & Madau 2007; Klypin, Trujillo-Gomez & Primack 2011; Reed et al. 2013; Dutton & Macciò 2014; Heitmann et al. 2016; Hellwing et al. 2016). However, the neglected role of baryons was uncertain and better cosmological tests would require baryonic physics to be included in the models and simulations.

Many solutions to the structure and abundance problems have been proposed since, some involving larger estimates of the mass of the MW, but most invoking a modification of the mass distribution of galactic satellite galaxies through a combination of tidal, ram-pressure stripping, and stellar feedback (e.g. Zolotov et al. 2012; Brooks et al. 2013; Arraki et al. 2014; Brooks & Zolotov 2014; Sawala et al. 2016). Although baryonic effects are now considered to be important in testing predictions of small-scale cosmology, the details and importance of each effect are difficult to assess in a self-consistent manner because of the complexity of the physics involved, and the lack of convergence in the subgrid models used in hydrodynamics simulations.

Isolated dwarf galaxies are not subject to environmental transformations due to ram-pressure and tidal stripping, and hence offer a more direct and clean way of testing cosmological predictions at small scales. ΛCDM predicts the abundance of DM haloes to increase steeply with decreasing maximum circular velocity. This galactic velocity function (VF) is superior to other abundance probes because it requires no assumptions about the mapping between light and mass.

Surveys have shown that DM haloes expected to host galaxies are several times more numerous than observed dwarfs in the local Universe. This is the so-called CDM dwarf overabundance problem (Tikhonov & Klypin 2009; Zavala et al. 2009; Zwaan, Meyer & Staveley-Smith 2010; Papastergis et al. 2011, 2015; Trujillo-Gomez et al. 2011; Klypin et al. 2015; Bekeraitė et al. 2016). Klypin et al. (2015) recently used a volume-limited sample of galaxies in the Local Volume (LV) to infer the abundance of DM haloes assuming that the observed H I velocity width of galaxies is the same as the maximum circular velocity of their host halo. Other authors have challenged this assumption and find instead that a large correction is necessary (Brook & Shankar 2016; Macciò et al. 2016).

In this paper, we develop a novel method to obtain the maximum circular velocity from the observed line-of-sight velocity width using a large complementary sample of galaxies with high-quality measurements of their spatially resolved gas kinematics, including the faintest field galaxies studied to date. Using this correction, we calculate the abundance of observed galaxies as a function of $V_{\rm max}$. To make a direct comparison with the observations, we include simple models of baryonic effects in the theoretical CDM halo VF.

This paper is organized as follows. Section 2 describes the observational data samples and the selection criteria. In Section 3, we describe the method used to correct the observed VF from linewidths to halo maximum circular velocities. Section 4 provides functional fits to the abundance of galaxies as a function of $V_{\rm max}$, and examines the effects of feedback and reionization on the observed DM halo VF. We discuss our results and present our conclusions in Sections 5 and 6, respectively. Throughout the paper, we assume $H_0 = 70$ km s^{-1} Mpc^{-1} and the *Planck* cosmological parameters $\Omega_{\rm m} = 0.309$, $\Omega_{\rm bar} = 0.049$, and $\sigma_8 = 0.816$.

2 DATA AND METHODS

In this paper, we use two large and complimentary data sets of gas kinematics, stellar, and H I gas mass. The first one is a very deep volume-limited sample of galaxies in the LV. The LV catalogue contains spatially unresolved H I velocity profile widths, which do not provide the information necessary to fit DM halo density profiles. For this reason, we use in addition an extension of the Papastergis & Shankar (2016) sample of galaxies with spatially resolved H I kinematics to establish a link between the H I profile widths of the LV objects and the circular velocity of their host DM haloes. We define baryonic mass as the total stellar and cold gas mass $M_{\rm bar} = M_{\rm star} + (4/3)M_{\rm HI}$, including helium and neglecting molecular hydrogen.

2.1 LV sample

The LV sample is based on the Karachentsev, Makarov & Kaisina (2013) catalogue. The catalogue includes distances, photometry, H I mass estimates, and H I velocity widths for a volume-limited sample of galaxies with distances $D < 10$ Mpc from the Sun. The sample consists of ∼900 galaxies of all morphological types and is complete down to a limiting magnitude $M_B = -14$, 90 per cent complete down to $M_B = -13.5$ (or $V_{\rm los} \simeq 20$ km s^{-1}), and 50 per cent complete down to $M_B = -12$ (or $V_{\rm los} \simeq 13$ km s^{-1}; Klypin et al. 2015, hereafter K15). On average, assuming $\langle B - K \rangle = 2.35$ (Jarrett et al. 2003) and $M_*/L_K = 0.6$, the LV sample is missing 50 per cent of all galaxies below $M_{\rm bar} \simeq 2 \times 10^7 {\rm M}_\odot$, or equivalently, below a stellar mass $M_{\rm star} \simeq 6.3 \times 10^6 {\rm M}_\odot$.

A subset of 620 objects have both unresolved H I 50 per cent velocity profile width ($W50$) measurements, stellar and H I masses. Most of the late-type galaxies have $W50$ data. For galaxies with H I, the line-of-sight rotation velocity $V_{\rm los}$ is simply $W50/2$, while for those with no detected H I, we assume the relation for dispersion-dominated galaxies from K15, $V_{\rm los} = 70 \times 10^{-(21.5+M_K)/7}$ km s^{-1} if $M_K < -15.5$, and $V_{\rm los} = 10$ km s^{-1} otherwise. Although this estimate is more uncertain than direct $W50$ velocities, our results are unchanged if we remove these objects from the analysis since they comprise less than 10 per cent of the sample.

2.2 Spatially resolved kinematics sample

The second data set is an extensive compilation of spatially resolved H I kinematic measurements for 202 gas-rich isolated galaxies as compiled by Papastergis & Shankar (2016). All objects have outermost-point H I deprojected rotational velocities, $V_{\rm out} = V(r_{\rm out})$. However, several objects lack a measurement of their full rotation curve, especially in the case of the lowest mass dwarfs in our sample. All the galaxies in the sample have measurements of H I mass and stellar mass, and 178 have optical half-light radii. For those

Table 1. Summary of velocity definitions used in this work.

Symbol	Definition
$W50$	H I velocity width measured at 50 per cent of the peak flux
$V_{\rm los}$	Line-of-sight velocity obtained directly from the H I profile width, $W50/2$ (or from K15 for galaxies with no H I , see Section 2.1)
$V_{\rm rot}$	Deprojected line-of-sight velocity, $V_{\rm los}/(\sin i)$, where i is the inclination of the galaxy. Should not be confused with the actual rotation velocity of the gas
$V_{\rm out}$	Rotation velocity measured at $r_{\rm out}$, the outermost point in the H I rotation curve
$V_{\rm circ}$	Circular velocity of the DM halo hosting the galaxy, $\sqrt{GM(<r)/r}$
$V_{\rm max}$	Maximum value of the circular velocity of the halo

without half-light radii data, we use the fit to the relation between $r_{1/2}$ and $M_{\rm bar}$ from Bradford, Geha & Blanton (2015).

In addition to resolved kinematic data, all the objects also have measured 50 per cent H I profile linewidths, allowing for direct comparison with the LV data. The sample galaxies span the widest range of velocities and baryonic masses available to date for star-forming galaxies, extending down to $M_{\rm bar} \sim 10^6 {\rm M}_\odot$, which is near the completeness limit of the LV sample. For further details, we refer the reader to Papastergis & Shankar (2016) and references therein. From here on, we refer to this sample as 'P16'.

2.2.1 *Pressure support corrections*

The $V_{\rm out}$ measurements used in this work include corrections for pressure support, so as to recover the circular velocity at the outermost radius in the H I disc, $r_{\rm out}$. For a large fraction of our sample, the pressure support corrections were performed in the original references, based on the measured H I velocity dispersion and H I surface brightness profile of each object. For the 12 objects lacking a published pressure support correction, we apply a simple estimate of the form

$$V_{\rm out} \rightarrow \sqrt{V_{\rm out}^2 + 2\sigma^2}, \quad (1)$$

with $\sigma = 8$ km s^{-1}, following Papastergis & Shankar (2016). This form of the so-called asymmetric drift correction assumes a radially constant velocity dispersion $\sim$8 km s^{-1} in the outer parts of an H I disc with an exponential surface density profile and an outermost rotation measurement at a radius equal to two disc scale lengths. High-resolution 21 cm observations of dwarfs typically find small values of the mean H I gas velocity dispersion $\sim$6–12 km s^{-1} (Swaters et al. 2009; Oh et al. 2011, 2015; Warren et al. 2012; Stilp et al. 2013; Lelli, Verheijen & Fraternali 2014; Iorio et al. 2017), with even lower values in the outer discs (where the gas kinematics are probed in our analysis). High-resolution hydrodynamical simulations of isolated dwarfs also obtain small values for the gas velocity dispersion that are consistent with observations (Read et al. 2016b).

Pressure support corrections become most important for the lowest velocity galaxies in the sample, where gas turbulent motion becomes comparable to ordered rotation. However, the corrections are only applied to the subsample with no published measurements of velocity dispersion and, when applied, are generally small.[1] For a galaxy with a measured $V_{\rm out} = 20$ km s^{-1}, the asymmetric drift correction we apply is $\sim$3 km s^{-1}, while for a dwarf with $V_{\rm out} = 40$ km s^{-1}, the correction becomes smaller than 2 km s^{-1}.

[1] The choice of assumptions in the asymmetric drift correction could also affect our results; however, Read et al. (2016b) show that the effect on the recovered $V_{\rm max}$ is very small.

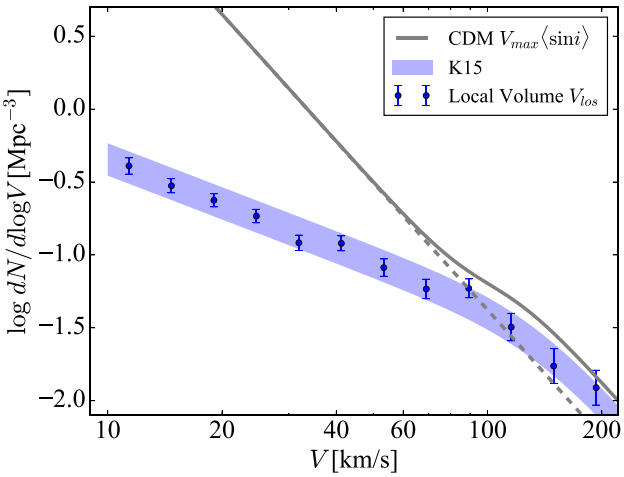

Figure 1. LV line-of-sight VF compared to the $V_{\rm max}$ VF of DM haloes predicted by CDM. The shaded area shows the fit provided by K15 including statistical uncertainty. The solid curve is the fit to simulations corrected for baryon infall by K15. The dashed line is the prediction without accounting for baryon infall. The CDM $V_{\rm max}$ VF includes a $\langle \sin i \rangle$ factor to account for projection on the sky assuming random galaxy inclinations.

Assuming instead an H I dispersion $\sigma = 12$ km s^{-1} would only increase the correction to $\sim$6 km s^{-1} for $V_{\rm out} = 20$ km s^{-1}, and $\sim$3 km s^{-1} for $V_{\rm out} = 40$ km s^{-1}. Due to the statistical nature of our method to obtain the $V_{\rm max}$ VF, the uncertainties in asymmetric drift corrections would only affect our results if they *systematically* underestimate the circular velocity.

Table 1 summarizes the velocity definitions adopted throughout the paper.

3 ANALYSIS

3.1 The galactic line-of-sight VF

The starting point for our analysis is the directly measured galactic line-of-sight VF, which is the number density of galaxies as a function of observed H I velocity width (or line-of-sight dispersion in the case of spheroidals). Fig. 1 shows the galactic line-of-sight VF in the LV and the $V_{\rm max}$ VF predicted by CDM structure formation. To allow a direct comparison, the halo $V_{\rm max}$ values were projected on to the line of sight by assuming uniformly random galaxy inclinations and multiplying the analytical halo VF by the factor $\langle \sin i \rangle = \sin(60)$. The figure shows essentially the same result as obtained by K15. However, K15 assumed that the correction from $V_{\rm los}$ to the halo $V_{\rm max}$ was negligible, resulting in a large discrepancy between the DM and galactic VFs observed in Fig. 1.

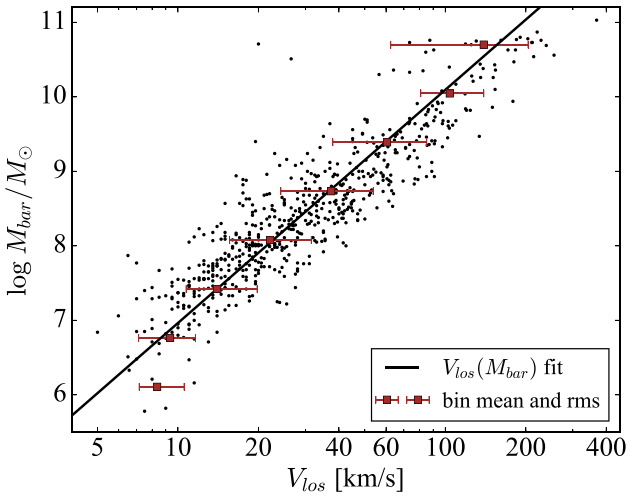

Figure 2. Line-of-sight rotation velocity and baryonic mass for galaxies in the LV sample. Squares with error bars represent the mean and standard deviation of the binned data. The line is a fit of the form $\log V_{\rm los}(M_{\rm bar}) = \alpha \log M_{\rm bar} + \beta$, treating $\log M_{\rm bar}$ as the independent variable and neglecting individual errors. Despite the large scatter, a linear fit provides a good description of the data, except perhaps for the faintest objects where data are scarce.

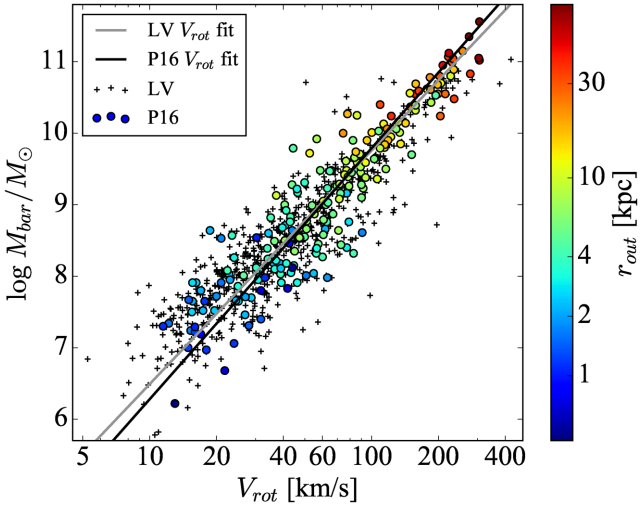

Figure 3. Comparison of the BTFR of the LV and the P16 sample. For a direct comparison with the LV data, we use the P16 rotation velocity obtained from the H I profile half-width, $V_{\rm rot} = W50/(2\sin i)$. For P16, the colour scale shows the radius of the outermost kinematic measurement for each galaxy and the solid line shows a linear regression treating $\log M_{\rm bar}$ as the independent variable and neglecting individual errors. The plus signs represent the LV sample and the dashed line its best linear fit. The two samples have nearly identical BTFRs while the P16 data appear to have smaller errors. These data will allow us to establish a connection between unresolved H I profile widths and spatially resolved rotation measurements in Section 3.3.

There are two possible ways to reconcile the observed VF with CDM. Either the rotation velocity of dwarf galaxies severely underestimates the halo maximum circular velocity or some physical process suppresses the formation of galaxies within DM haloes below $V_{\rm los} \sim 80$ km s^{-1}. In this section, we consider the first possibility. For this, we need to obtain the maximum circular velocity of each galaxy in the LV by fitting density profiles to kinematic data. However, this requires resolved kinematic data from targeted observations. Most objects in the LV sample do not have resolved kinematic data so we will need to relate the LV sample linewidths with the resolved rotation velocities of the selected P16 sample.

Our objective here is to find the relation between the galaxy VF and the VF of the host DM haloes. Fig. 2 shows the total baryonic mass versus $V_{\rm los}$ for the LV sample. The distribution of line-of-sight velocities, correcting for incompleteness as in K15, yields the galaxy VF.

To obtain an unbiased description of the relation between $M_{\rm bar}$ and $V_{\rm los}$, we calculate the distribution of the line-of-sight velocities in bins of $\log M_{\rm bar}$. Fig. 2 shows that the resulting binned data can be appropriately described by a linear fit of the form[2]

$$\log V_{\rm los}^{LV} = \alpha \log M_{\rm bar} + \beta, \quad (2)$$

with $\alpha = 0.319$ and $\beta = -1.225$, and a correlation coefficient $r = 0.897$. Having shown that the line-width baryonic Tully–Fisher relation (BTFR) of the LV sample is well described by a linear model, we can proceed to relate the line-of-sight H I velocity to the resolved kinematic measurements necessary for fitting DM halo mass profiles.

3.2 H I linewidths and resolved measures of galactic rotation

Similarly to Brook & Shankar (2016), our method relies on directly relating various galaxy kinematic measures via the observed tight coupling with total baryon mass (i.e. the BTFR). The scaling between measures of gas rotation and baryonic mass has been shown to span a large range of masses from dwarfs to giant discs with very little scatter regardless of whether profile widths or spatially resolved rotation measures are used (McGaugh 2012; Papastergis, Adams & van der Hulst 2016). Exploiting the relatively small and well-understood systematic errors in the cold baryonic masses of isolated dwarfs (which tend to be gas dominated), we can *statistically* connect the profile widths of LV objects to the outermost resolved rotation measurement, $V_{\rm out}$, of the P16 sample and the corresponding average $V_{\rm max}$ of their host DM haloes.

In this section, we begin with the first step in this method by quantifying the *average* relation between H I linewidth-derived rotation velocity, ($V_{\rm rot}$), and ($M_{\rm bar}$). This will then allow us to connect $V_{\rm rot}$ to $V_{\rm max}$ using the P16 sample and profile fitting to infer the average $V_{\rm out}$–$V_{\rm max}$ relation in Section 3.3.[3] Although there is a tendency to overestimate inclination corrections for low-inclination galaxies, we verified that this effect is small and has a negligible effect on our results.

Fig. 3 compares the relation between baryonic mass and deprojected line-of-sight velocity, $V_{\rm rot} = W50/(2\sin i)$, in the P16 and LV

[2] In this fit and throughout the paper when modelling the observed relation between $M_{\rm bar}$ and velocity, we treat $\log M_{\rm bar}$ as the independent variable and velocity as the dependent variable, assuming that the velocities dominate the uncertainty. We further neglect the observational errors in the individual velocities and perform unweighted linear regressions to prevent biasing the fits towards the massive galaxies that have the smallest logarithmic velocity errors.

[3] An alternative way to obtain the mean linewidth-derived rotation velocities of the LV galaxies, $V_{\rm rot}$, is to assume the average deprojection for randomly sampled orientations, $V_{\rm rot} = V_{\rm los}/\langle \sin i \rangle \approx 1.3 V_{\rm los}$. However, since the LV catalogue includes measured inclinations, we opted to use the individually deprojected linewidths. This becomes particularly important for the lowest mass dwarfs as their counts are not large enough to properly sample the expected distribution of inclinations.

samples. The P16 rotation velocities are well described by a linear model of the form

$$\log V_{\rm rot}^{\rm P16}(M_{\rm bar}) = \delta \log M_{\rm bar} + \gamma, \quad (3)$$

with $\delta = 0.289$ and $\gamma = -0.803$, and correlation coefficient $r = 0.956$.[4] We tested the linearity assumption and confirmed that power-law fits describe the data as well as non-parametric models (see Appendix B). Within the fitting uncertainties, the LV data are consistent with the same BTFR.[5] Here we assume that equation (3) (black line in Fig. 3) represents the general galaxy population more accurately than the LV fit (grey line) due to the more precise inclination estimates obtained from the gas kinematic models used to derive rotation curves. However, this choice does not affect the results of our analysis.

The careful reader might notice that equation (3) is different from the expected deprojection of equation (2) assuming random orientations, $V_{\rm rot} = V_{\rm los}/\langle \sin i \rangle$. In general, the average $V_{\rm rot}$ (at fixed $M_{\rm bar}$) follows this geometric correction for massive discs but is larger than $V_{\rm los}/\langle \sin i \rangle$ for the P16 dwarf galaxies. Papastergis & Shankar (2016) argue that this bias is due to the intrinsic thickness of the H I discs of dwarfs causing an underestimate of their true inclination in low-i objects and therefore an *overestimate* of the $1/\sin i$ factor in the deprojected rotation. Only the low-i dwarfs are affected by this bias, but the sample mean also shifts systematically towards higher values of $V_{\rm rot}$. This explanation is confirmed by the comparison with high-inclination (and therefore more accurate) subsamples in Appendix A. In our analysis, we choose not to correct for this effect since it would simply shift the VF towards even lower $V_{\rm max}$ at dwarf scales, enhancing the discrepancy with CDM.

In modelling these data, we explicitly assume that for a given baryonic mass the LV and the P16 galaxies inhabit the same DM haloes and that systematic deviations in the observed rotation velocities are due to differences in H I content and extent that arise naturally from galaxy formation. This assumption allows us to obtain an estimate of the maximum linewidth-derived $V_{\rm rot}$ of an LV galaxy. Using equations (2) and (3), and setting $\langle \log V_{\rm rot}^{\rm LV} \rangle = \langle \log V_{\rm rot}^{\rm P16} \rangle$ as justified by Fig. 3, gives

$$\langle \log V_{\rm rot}^{\rm LV} \rangle = \langle \log V_{\rm los}^{\rm LV} \rangle + \log \Delta, \quad (4)$$

where

$$\log \Delta = (\delta - \alpha) \log M_{\rm bar} - (\gamma - \beta), \quad (5)$$

and the brackets denote population averages over narrow ranges of baryonic mass.

3.3 Connecting H I kinematics to DM halo circular velocities

In the previous section, we obtained a statistical correction to calculate the linewidth-derived rotation velocity $V_{\rm rot}$ at a given line-of-sight velocity $V_{\rm los}$ for LV galaxies. The next step is to find a relation between the $V_{\rm rot}$ of the P16 galaxies and the maximum circular velocity of their host DM haloes.

DM-only N-body simulations in the standard ΛCDM cosmology show that haloes have a density profile well described by the NFW parametrization (Navarro, Frenk & White 1997):

$$\rho(r) = \frac{\rho_0}{\frac{r}{r_{\rm s}}\left(1 + \frac{r}{r_{\rm s}}\right)^2}, \quad (6)$$

with

$$r_{\rm s} = R_{\rm vir}/c \quad (7)$$

and

$$R_{\rm vir} = \left(\frac{3M_{\rm vir}}{4\pi \Delta_{\rm vir} \rho_{\rm m}}\right)^{1/3}, \quad (8)$$

where $x = r/R_{\rm vir}$, and $\Delta_{\rm vir} \approx 335$, and $\rho_{\rm m} = 1.36 \times 10^2 \Omega_{\rm m}$ $\mathrm{M}_\odot$ kpc^{-3} are the virial overdensity and the matter density at present, respectively. Once the concentration is specified, the NFW profile is uniquely defined for a given $M_{\rm vir}$. To obtain the virial mass, we solve the equation for the circular velocity

$$V_{\rm circ}(r) = V_{\rm vir}\left[x \frac{\ln(1+cx) - \frac{cx}{1+cx}}{\ln(1+c) - \frac{c}{1+c}}\right]^{1/2}, \quad (9)$$

and

$$V_{\rm vir} = \left(\frac{GM_{\rm vir}}{R_{\rm vir}}\right)^{1/2}, \quad (10)$$

where $x = r/r_{\rm s}$. We solve numerically the equation[6]

$$V_{\rm circ}(r_{\rm out}, M_{\rm vir}, c(M_{\rm vir})) = V_{\rm out}, \quad (11)$$

for $M_{\rm vir}$, where $c(M_{\rm vir})$ is obtained from the average concentration–mass relation (Dutton & Macciò 2014)

$$\log c(M_{\rm vir}) = 1.025 \left(\frac{M_{\rm vir}}{10^{12}\, h^{-1}\, \mathrm{M}_\odot}\right)^{-0.097}. \quad (12)$$

We then obtain the maximum circular velocity[7]

$$V_{\rm max} = V_{\rm circ}(r_{\rm max}), \quad (13)$$

where $r_{\rm max} \approx 2.16 r_{\rm s}$ for the NFW profile. For an estimate of the uncertainty in the $V_{\rm max}$, we repeat the same calculation for the extreme values of $V_{\rm out}$ and concentration:

$$V_{\rm out}^{\pm} = V_{\rm out} \pm \sigma_{V_{\rm out}} \quad (14)$$

and

$$\log c^{\pm} = \log c(M_{\rm vir}) \mp \sigma_{\log c}, \quad (15)$$

where $\sigma_{\log c} = 0.11$ is the standard deviation in the concentration–mass relation (Dutton & Macciò 2014), and $\sigma_{V_{\rm out}}$ is the reported measurement error in $V_{\rm out}$. This gives a 1σ upper limit to the maximum and minimum circular velocity of a halo that could host a galaxy with a given measured $V_{\rm out}$.

In Appendix C, we show that the results presented here do not depend on the relative baryonic contribution to the rotation velocity,

[4] For consistency, the numerical values of these parameters were obtained from a fit to the same P16 subsample used for the profile fitting in Section 3.3. The two fits are almost identical within the uncertainties and this choice has a negligible effect on our results.

[5] In Appendix A, we show that the BTFRs of the two samples are also equivalent when inclination uncertainties are minimized by selecting only high-inclination objects.

[6] Since massive galaxies are known to have a non-negligible baryonic contribution to their rotation curve, we subtract the enclosed baryonic mass $V_{\rm out} \rightarrow \sqrt{V_{\rm out}^2 - GM_{\rm bar}/r_{\rm out}}$ when $V_{\rm out} > 100$ km s^{-1}. This assumes that the entire baryonic mass of the galaxy is contained within $r_{\rm out}$. The approximation is valid since by definition $r_{\rm out}$ occurs near the edge of the H I disc and H I is typically more extended than the stars.

[7] For massive galaxies with $V_{\rm out} > 100$ km s^{-1}, we add the baryon mass to the DM fit, $V_{\rm max} = \sqrt{V_{\rm circ}^2(r_{\rm max}) + GM_{\rm bar}/r_{\rm max}}$.

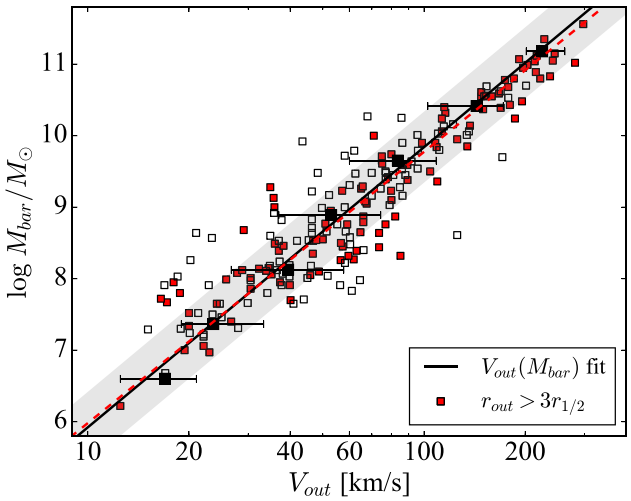

Figure 4. Dependence of the *resolved* P16 BTFR on the relative extent of the resolved kinematic measurements. Here the rotation velocity $V_{\rm out}$ is measured at the outermost kinematic radius, $r_{\rm out}$. The blue points show the selected subsample with the most extended kinematic data, $r_{\rm out} > 3r_{1/2}$. The dashed line shows a linear regression including only the selected P16 data, while the solid line and the shading show the fit to the full sample and the scatter. The points with error bars denote the binned means and scatter of the full sample in uniform logarithmic mass bins. The regressions treat $\log M_{\rm bar}$ as the independent variable and neglect individual errors. Both samples are well described by power laws. The selected sample of galaxies with the most extended kinematic data follows the same BTFR as the complete P16 sample.

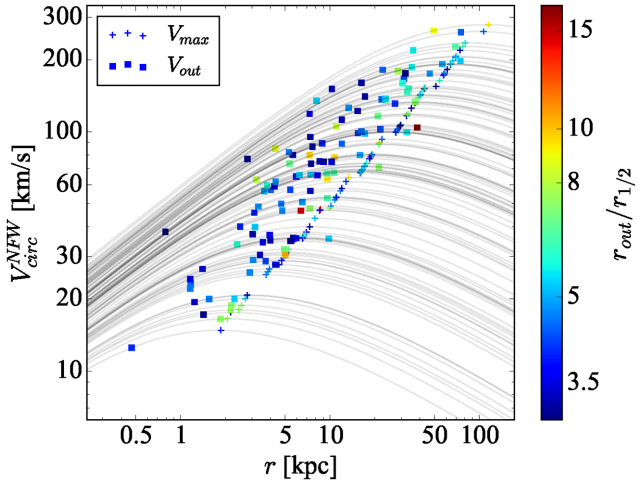

Figure 5. NFW DM circular velocity profile fits to the selected P16 subsample. Solid curves show the individual profiles calculated using equation (9). The maximum circular velocity of the DM halo is indicated by a plus sign while the outermost resolved kinematic point is represented by a square. Error bars are omitted for clarity.

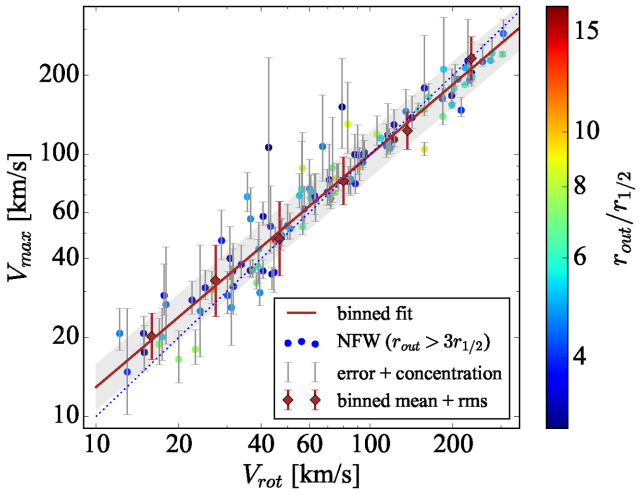

Figure 6. Galaxy maximum circular velocity $V_{\rm max}$ as a function of observed inclination-corrected line-of-sight velocity in the P16 selected subsample. Circles with thin error bars represent individual galaxies and their total uncertainties (due to measurement and concentration, equations 14 and 15). The colour scale shows the resolved kinematic extent relative to the half-light radius. Diamonds with thick error bars denote the mean and standard deviation of the error-weighted $V_{\rm max}$ values in uniform $\log V_{\rm rot}$ bins. The solid line is a linear fit to the binned data treating the binned error-weighted mean $\log V_{\rm max}$ values as the dependent variable and neglecting the scatter in individual bins. The shaded area shows the scatter in $V_{\rm max}$. The dotted line indicates the relation $V_{\rm max} = V_{\rm rot}$.

$(GM_{\rm bar}/r_{\rm out})/V_{\rm out}^2$. Additionally, to guarantee that the DM profiles have not been modified by core formation due to stellar feedback (e.g. Mashchenko, Wadsley & Couchman 2008; Governato et al. 2012; Pontzen & Governato 2012; Di Cintio et al. 2014; Tollet et al. 2016; Read, Agertz & Collins 2016a), we further limit the sample to galaxies with $r_{\rm out} > 3r_{1/2}$. According to Read et al. (2016a), the DM distribution should remain unaffected by feedback at $r \gtrsim 2r_{1/2}$. About 100 galaxies remain in the sample after these selection criteria are applied. The cuts do not significantly affect the main results of the paper (see Appendix A).

Fig. 4 shows the BTFR of the P16 sample using $V_{\rm out}$ as a probe of rotation velocity. In this case, the correlation is also tight, with a scatter $\sigma_{\log V_{\rm out}} = 0.13$ around a linear fit. As expected, this is larger than the scatter found in other BTF samples that make stringent cuts based on the shape and extent of the rotation curves (e.g. McGaugh 2012; Lelli, McGaugh & Schombert 2016). A fit using only galaxies in the subsample with $r_{\rm out} > 3r_{1/2}$ is essentially identical, within the uncertainties, to the full sample fit. This demonstrates that galaxies with gas discs of relatively different extent all follow the same relation between baryonic mass and rotation velocity. In other words, there is no systematic bias in the selection of the subsample used for density profile fitting.

The DM halo profiles obtained for the P16 subsample are shown in Fig. 5, and the relation between the inclination-corrected H I 50 per cent half-width and $V_{\rm max}$ is shown in Fig. 6. In several galaxies, the fitted circular velocity profile reaches $V_{\rm max}$ at or near the outermost kinematic radius. However, for many, the profile keeps rising and the maximum can be at several times $r_{\rm out}$. Fig. 5 shows that the difference between $V_{\rm out}$ and $V_{\rm max}$ is in general small but not negligible. Thus, the assumption by K15 that the difference between $V_{\rm rot}$ and $V_{\rm max}$ is less than 30 per cent applies generally and agrees with our conclusions.

In Fig. 6, we also indicate the total uncertainties from measurement error as well as halo concentration as error bars. To avoid biases, we calculate the statistics of the error-weighted data in uniform $\log V_{\rm rot}$ bins and perform a fit to the mean $V_{\rm max}$ of the

binned data. The data are well described by a linear model of the form[8]

$$\langle \log V_{\rm max} \rangle = \zeta \langle \log V_{\rm rot}^{\rm P16} \rangle + \eta, \quad (16)$$

with $\zeta = 0.887$ and $\eta = 0.225$ and rms scatter $\sigma_{V_{\rm max}} = 0.09$. As expected, massive galaxies with $V_{\rm rot} > 80$ km s^{-1} are well fitted by haloes with $V_{\rm max}$ close to the measured inclination-corrected H I profile half-width. For lower mass galaxies, the H I gas does not seem to extend far enough to probe the maximum circular velocity of the halo, resulting in a larger correction as $V_{\rm rot}$ decreases. The mean correction is less than 5 km s^{-1} for dwarf galaxies with $V_{\rm rot} \approx 12$ km s^{-1}.

The result of Fig. 6 can now be used to re-express the observed VF of the LV in terms of the $V_{\rm max}$ of the haloes hosting the LV galaxies. We refer to this distribution as the 'galactic $V_{\rm max}$ function'. Using equations (4) and (16), we can derive a *statistical* relation between the line-of-sight rotation velocity of a galaxy in the LV and its maximum circular velocity,

$$\langle \log V_{\rm max}^{\rm LV} \rangle = \langle \log V_{\rm los}^{\rm LV} \rangle + \Lambda \langle \log M_{\rm bar} \rangle + \Psi, \quad (17)$$

where

$$\Lambda = \zeta\delta - \alpha = -0.0626 \quad (18)$$

and

$$\Psi = \zeta\gamma + \eta - \beta = 0.738, \quad (19)$$

and angled brackets denote population means over narrow logarithmic $M_{\rm bar}$ bins.

4 RESULTS

4.1 The abundance of galaxies as a function of their host halo $V_{\rm max}$

Equation (17) allows us to assign a $V_{\rm max}$ to each object in the LV based on detailed modelling of the density profiles of the P16 sample galaxies. To obtain the $V_{\rm max}$ VF of the LV, we apply the following procedure.

(i) Using $V_{\rm los}$ and $M_{\rm bar}$ for each LV galaxy to obtain $V_{\rm rot}$ using equation (4).
(ii) Using $V_{\rm rot}$ and equation (16) to obtain $V_{\rm max}$ for each galaxy.
(iii) Calculate the number density of LV galaxies as a function of the $V_{\rm max}$ assigned to each object including the completeness correction from K15.

In the procedure above, steps 1 and 2 are equivalent to solving equation (17) for each galaxy.

Although we apply this correction to each object individually, the resulting $V_{\rm max}$ is only meaningful in a statistical interpretation when an ensemble average is calculated. A caveat of this approach is that it neglects the intrinsic scatter in the BTFRs. It is possible to repeat our analysis by modelling the scatter analytically in equation (17). However, our method is simpler and does not require assumptions about the error distributions. Furthermore, adding scatter to the VF does not alter its slope as long as the scatter does not depend on velocity (Papastergis et al. 2011).

[8] Here we treat $V_{\rm max}$ as the dependent variable and $V_{\rm rot}$ as the independent variable and neglect the dominant uncertainties in $V_{\rm max}$ when performing the linear regression to avoid overweighting the massive galaxies. Inverting the direction of the fit has negligible effects on the result.

Fig. 7 shows our main result, the $V_{\rm max}$ VF in the LV. The distribution is well fitted by a Schechter function of the form

$$\Phi(V_{\rm max}) = \frac{{\rm d}N}{{\rm d}\log V_{\rm max}} = \phi^* \left(\frac{V_{\rm max}}{V^*}\right)^p \exp\left[-\left(\frac{V_{\rm max}}{V^*}\right)^q\right], \quad (20)$$

with $\phi^* = 2.72 \times 10^{-2}$ Mpc^{-3}, $V^* = 2.50 \times 10^2$ km s^{-1}, $p = -1.13$, and $q = 3.14$. This fit is also shown in Fig. 7. The $V_{\rm max}$ function is slightly steeper than the observed $V_{\rm los}$ VF but still shallower than the CDM VF because the difference between the halo $V_{\rm max}$ and the measured rotation velocity is small and increases as galaxy mass decreases. The galactic $V_{\rm max}$ function we obtain here should be used as a benchmark for any structure formation model to reproduce in order to be considered successful at small scales. In the next section, we evaluate the effects of baryonic processes on the theoretical CDM VF to determine its ability to predict the abundance of small structures.

4.1.1 *The effect of feedback-induced cores on the observed* $V_{\rm max}$ *function*

Galaxy formation simulations with very efficient supernova feedback implementations typically produce dwarf galaxies with DM density profiles that are shallower than NFW in the inner few kiloparsecs (e.g. Mashchenko et al. 2008; Governato et al. 2010, 2012; Pontzen & Governato 2012; Teyssier et al. 2013; Di Cintio et al. 2014; Oñorbe et al. 2015; Trujillo-Gomez et al. 2015; Read et al. 2016a; Tollet et al. 2016). However, the details of the transformation are still a matter of debate. For example, Di Cintio et al. (2014) parametrize the core-creation efficiency solely as a function of the ratio $M_{\rm star}/M_{\rm halo}$, while Oñorbe et al. (2015) and Read et al. (2016a) find that it also depends on the star formation history of the galaxy. The extent and slope of the DM core is also currently under debate.

Recently, Read et al. (2016a) found that the effect of supernova feedback is converged once the resolution is high enough to properly capture the expansion of the blastwave. They provide a general modification of the NFW profile,

$$M_{\rm coreNFW}(<r) = M_{\rm NFW}(<r) \times \left[\tanh\left(\frac{r}{r_{\rm c}}\right)\right]^n, \quad (21)$$

where

$$n = \tanh\left(\kappa \frac{t_{\rm SF}}{t_{\rm dyn}}\right), \quad (22)$$

and $t_{\rm SF}$ and $t_{\rm dyn}$ are the total star formation time and the circular orbit time at the NFW scale radius, respectively. Their simulations are well fitted with $\kappa = 0.04$. Furthermore, Read et al. (2016b) show that this 'coreNFW' profile fits 'problematic' rotation curves within CDM. For an effectively flat core, the parameter $t_{\rm SF} \gg t_{\rm dyn}$ and $n = 1$. The core radius is proportional to the projected stellar half-mass radius, $r_{\rm c} = 1.75 R_{1/2}$. The circular velocity of the coreNFW profile becomes

$$V_{\rm circ}^{\rm coreNFW}(r) = V_{\rm circ}^{\rm NFW}(r) \times \left[\tanh\left(\frac{r}{r_{\rm c}}\right)\right]^{n/2}. \quad (23)$$

We repeat the same profile-fitting procedure from Section 3.3 replacing equation (11) with

$$V_{\rm circ}^{\rm coreNFW}(r_{\rm out}, M_{\rm vir}, c(M_{\rm vir})) = V_{\rm out}, \quad (24)$$

and solving for $M_{\rm vir}$ while assuming that $R_{1/2}$ is equal to the half-light radius for each galaxy. In Appendix D, we show that the particular choice of cored profile parametrization has no effect on our results.

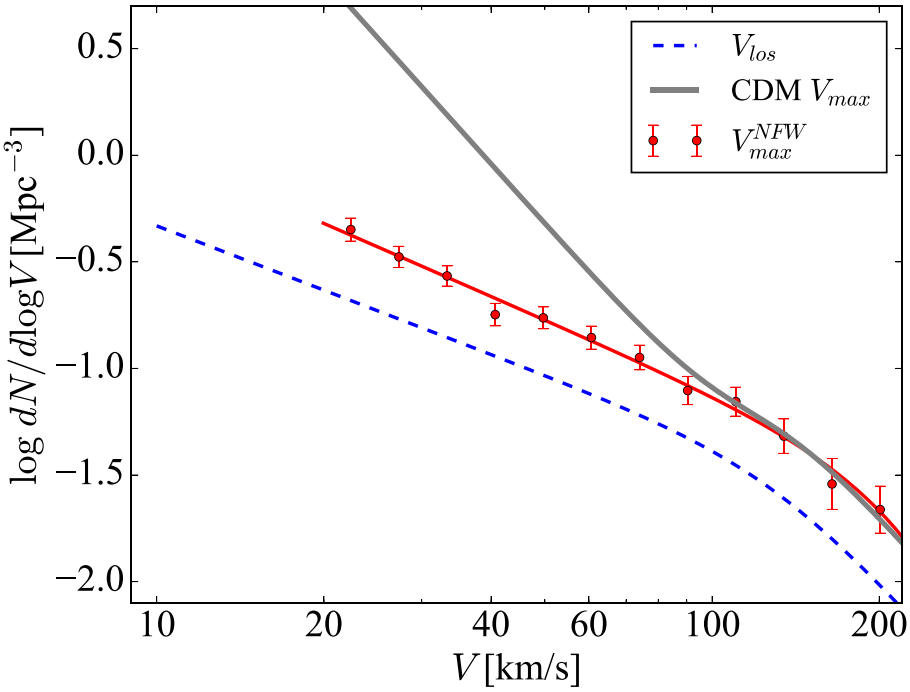

Figure 7. Galactic $V_{\rm max}$ function of the LV. Points with error bars denote the distribution obtained by using equation (17) to calculate the $V_{\rm max}$ of each galaxy in the LV sample. The solid curve is a Schechter fit to the distribution (see equation 20). The dashed curve is the observed $V_{\rm los}$ function. The grey curve is the parametrization of the theoretical CDM VF from K15.

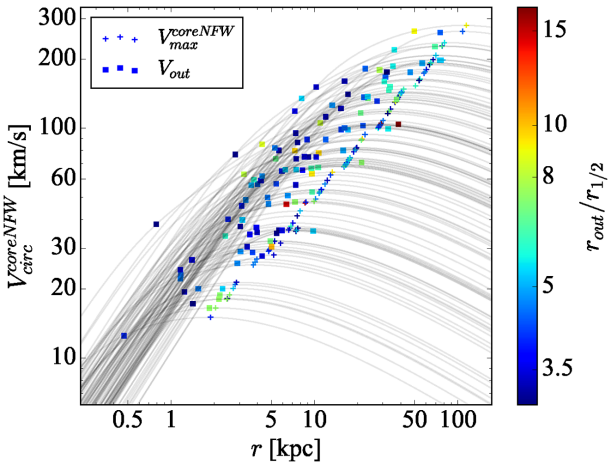

Figure 8. Same as Fig. 6 but for cored NFW profiles obtained using the prescription from Read et al. (2016a).

Fig. 8 shows the resulting cored DM halo fits. Although the central circular velocities are reduced with respect to Fig. 5 due to the presence of a core, the maximum circular velocity of the haloes stays relatively unchanged. This is a result of our selection of the P16 subsample with $r_{\rm out} > 3r_{1/2}$. We emphasize here that these fits represent an extreme case where all galaxies form the most extreme shallow DM cores seen in simulations irrespective of their stellar mass. These $V_{\rm max}$ values thus represent upper limits to the effect of feedback on the $V_{\rm max}$ VF in our analysis.

Fig. 9 shows the $V_{\rm max}$–$V_{\rm rot}$ relation of the selected P16 galaxies assuming extreme feedback-induced cores.

The result is essentially unchanged from Fig. 7 because of the cut we imposed on the relative kinematic radius of the data. Ensuring that $r_{\rm out} > 3r_{1/2}$ selects galaxies for which a DM core does not modify the rotation velocity at the outermost kinematic data point.

It should be noted that fitting cored profiles to galaxies with smaller $r_{\rm out}/r_{1/2}$ would allow some dwarfs with small kinematic radii to be placed in very massive haloes. This occurs because at a fixed circular velocity in the inner region, a cored profile will allow for a slowly rising rotation curve with a larger $V_{\rm max}$ and $M_{\rm vir}$ (see e.g. Papastergis & Shankar 2016). These solutions lead to extreme outliers in Fig. 9 with large uncertainties in halo mass. We verified that most of the $V_{\rm max}$ values of dwarfs with $r_{\rm out} < 3r_{1/2}$ follow the relation in Fig. 9, while a few dwarfs get fitted to profiles with a $V_{\rm max}$ more than twice larger than $V_{\rm rot}$. This has a negligible effect on the best-fitting $V_{\rm max}$–$V_{\rm rot}$ relation (equation 16). Moreover, we believe that the cut $r_{\rm out} > 3r_{1/2}$ provides more reliable cosmological constraints because it probes the unmodified part of the DM halo where, in addition, baryons make a negligible mass contribution.

We have shown that observational effects and DM halo cores cannot account for the large discrepancy in the abundance of LV galaxies compared to CDM haloes. However, theoretical work has shown that other important effects should be included when computing the theoretical abundance of galaxies hosted by DM haloes. In the following section, we evaluate the effects of baryon depletion due to stellar feedback and photoheating due to the reionization of the Universe.

4.2 The impact of stellar feedback and reionization on the observed galaxy abundance

It is expected that once the Universe becomes reionized at redshift $z \sim 6$, the background ultraviolet radiation field from galaxies and quasars will have a strong effect of the formation of the faintest dwarf galaxies. In DM haloes with shallow potential wells, cold

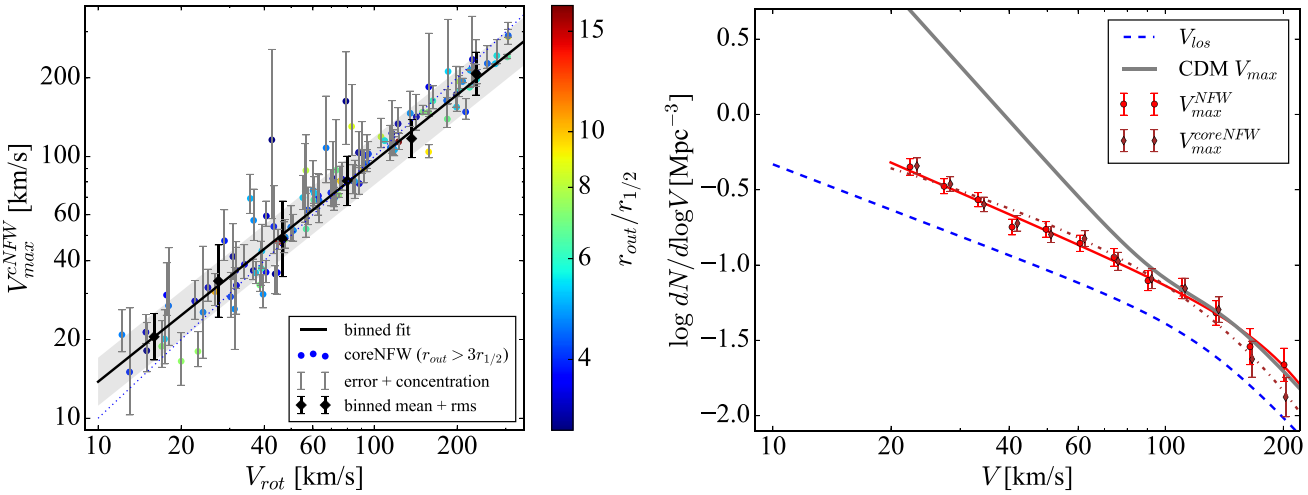

Figure 9. Left: same as Fig. 6 assuming that all haloes have flat inner cores resulting from stellar feedback. The selection of galaxies with $r_{\rm out} > 3r_{1/2}$ ensures that the core has little effect on the resulting $V_{\rm max}$ compared to NFW profiles (see Fig. 5). Right: Galactic $V_{\rm max}$ function of the LV including the effects of feedback-induced cores on density profiles. Diamonds show the result of assuming maximum cores in the coreNFW parametrization from Read et al. (2016a). Squares reproduce the result in Fig. 7, which assumes NFW profiles. The dot–dashed and solid curves are Schechter fits to the NFW and coreNFW points, respectively. The grey curve is the parametrization of the CDM halo VF from K15.

neutral hydrogen will be ionized and heated. The ionized gas could then escape the halo and leave a 'dark galaxy' behind. These dark galaxies may contain few to no stars depending on the time-scales of accretion, photoevaporation, and star formation.

Although a complete modelling of the process is extremely difficult, simplified simulations have shown that the total baryonic mass of the halo at $z = 0$ is sharply suppressed for masses below a characteristic scale $M_{\rm vir} \sim 10^{9.5}$ M$_\odot$ (Okamoto et al. 2008). The imprint of the transition should be detectable in galaxy samples of the smallest field dwarfs known to date. Therefore, the P16 sample is ideal to search for the signature of this process.

Since photoevaporation might also affect other galaxy properties such as the extent of the H I disc, it is important to relate the baryonic mass to the depth of the potential well, using $V_{\rm max}$. Fig. 10 shows $M_{\rm bar}$ versus $V_{\rm max}$ obtained using NFW profile fitting (see Section 3.3). Two processes should be dominant in setting this relation: loss of gas due to feedback-produced outflows and photoevaporation due to an external UV field. The physics of these processes is quite different and there is no reason to expect a simple linear scaling of the baryon mass with halo circular velocity (in logarithmic units). A second-order polynomial least-squares fit of the form $\log V_{\rm max} = a_1 \log M_{\rm bar}^2 + a_2 \log M_{\rm bar} + a_3$ yields a negligible quadratic term, indicating that the data favour a nearly perfect linear relation between maximum circular velocity and baryonic mass.

To obtain a limit on the maximum amount of baryonic loss supported by the data, we fit a no-suppression linear model of the form

$$\log V_{\rm max}^{\rm nosup}(M_{\rm bar}) = a \log M_{\rm bar} + b, \tag{25}$$

as well as model with a baryonic mass suppression term,

$$V_{\rm max}^{\rm sup}(M_{\rm bar}) = f_{\rm sup}(M_{\rm bar}) \times V_{\rm max}^{\rm nosup}(M_{\rm bar}), \tag{26}$$

where

$$f_{\rm sup}(V_{\rm max}) = 0.5 \left[1 + {\rm erf}\left(\frac{\log V_{\rm max} - \log V_0}{\log \sigma_0}\right)\right]. \tag{27}$$

Here, V_0 is the $V_{\rm max}$ value where the baryonic mass is reduced by 50 per cent relative to the no-suppression model, and σ_0 is the

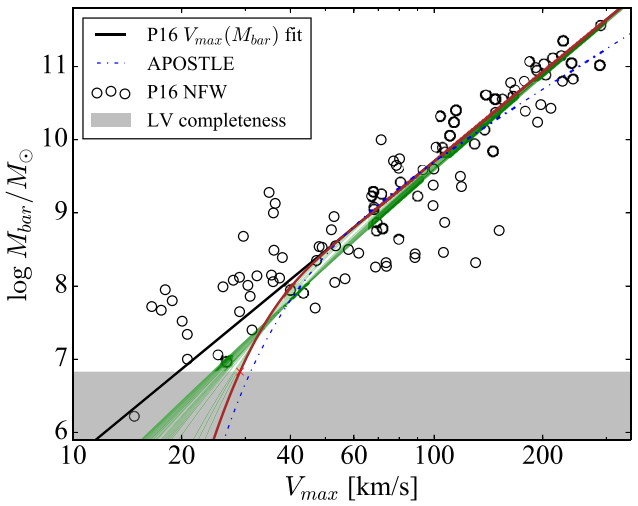

Figure 10. Relation between cold baryonic mass and $V_{\rm max}$ for the selected P16 galaxies. The straight line shows the no-suppression model in the form of a linear relation. The thin curves show the most extreme fits to the suppression model (equation 26) that are within the 3σ allowed region when $V_{\rm crit}$ and $\sigma_{\rm crit}$ are allowed to vary freely. The shaded area shows the completeness limit of the LV sample. The thick curve corresponds to the suppression model with the strongest effect on the observable galaxy VF. The 'x' marks the value $V_{\rm crit}$ at which half of the galaxies in the LV are undetected in the maximum suppression scenario. The dash–dotted line reproduces the results of the APOSTLE simulation (Sales et al. 2017).

width of the transition. We assume that a very sharp transition is unphysical and limit the width to $\log(\sigma_0/{\rm km\ s^{-1}}) > 1.2$, similar to the value found by Okamoto et al. (2008). Fig. 10 shows the results for both models. Since the model with suppression has two free parameters, we show a family of fits that are 3σ away from the no-suppression model using a likelihood ratio analysis. To do this, the suppression models are explored by sampling a grid of points in

a two-dimensional parameter space defined by σ_0 and V_0, for which the likelihood is assumed to be

$$\mathcal{L} = \prod_{i=1}^{N} \frac{1}{\sqrt{2\pi\sigma^2}} \exp\left[-\frac{\left(V_{\mathrm{max},i} - V_{\mathrm{max}}^{\mathrm{fit}}(M_{\mathrm{bar},i})\right)^2}{2\sigma^2}\right], \quad (28)$$

where N is the number of data points, σ is the variance of the V_{max} data with respect to the fit, and the subscript *fit* refers to either the linear fit (equation 25) or the fit with suppression (equation 26). The log-likelihood becomes

$$\ln\mathcal{L} = -\frac{N}{2}\ln\sigma^2 - \frac{1}{2\sigma^2}\sum_{i=1}^{N}\left[V_{\mathrm{max},i}^2 - V_{\mathrm{max}}^{\mathrm{fit}}(M_{\mathrm{bar},i})\right]^2. \quad (29)$$

The logarithm of the likelihood ratio will be chi-squared distributed,

$$\chi^2_{\mathrm{sup}} = -2\ln\frac{\mathcal{L}_{\mathrm{sup}}}{\mathcal{L}_{\mathrm{nosup}}}. \quad (30)$$

Models with a χ^2_{sup} corresponding to a p-value of 0.003 (with 2 degrees of freedom) are selected and shown in Fig. 10 as thin curves. The curve with the most extreme downward bend (thick curve) is chosen as the maximum suppression model.

The next step to obtain the modified VF is to calculate the number of galaxies that are detected in surveys as a function of V_{max} and their maximum suppressed baryonic content. Assuming that the scatter in the M_{bar}–V_{max} relation is Gaussian, the detected abundance will be reduced by half at $V_{\mathrm{max}} = V_{\mathrm{crit}}$, and the functional shape of the transition will be described by an error function of the form

$$\mathcal{F}_{\mathrm{ext}}(V_{\mathrm{max}}) = 0.5\left[1 + \mathrm{erf}\left(\frac{\log V_{\mathrm{max}}^{\mathrm{sup}} - \log V_{\mathrm{crit}}}{\sqrt{2}\sigma_{\log V_{\mathrm{max}}}}\right)\right], \quad (31)$$

where $M_{\mathrm{bar}}^{\mathrm{sup}}$ is given by equation (26), $\sigma_{\log V_{\mathrm{max}}} = 0.14$ is the logarithmic scatter in V_{max} around the linear fit, and V_{crit} is the value of V_{max} at which 50 per cent of the galaxies would be undetectable in the LV. Using the 50 per cent completeness B-band magnitude of the LV (see Section 2.1) gives the stellar mass completeness limit, $M_{\mathrm{lim}} = 10^{6.8}\,\mathrm{M}_\odot$. To include galaxies with low gas fractions, we assume that the baryonic mass completeness limit is equal to this value. Due to the steepness of the reionization downturn (see Fig. 10), the precise value of M_{lim} would not significantly affect the theoretical predictions.

In addition to photoevaporation, DM haloes hosting star formation and energetic feedback from supernovae and stellar radiation may lose a significant fraction of their baryons through massive gas outflows (e.g. Governato et al. 2010; Brook et al. 2011; Munshi et al. 2013; Shen et al. 2014; Oñorbe et al. 2015; Trujillo-Gomez et al. 2015; Wang et al. 2015; Wheeler et al. 2015). This effect has been observed in simulations where feedback is tuned to reproduce the observed stellar mass function (Sawala et al. 2015). The loss of baryons at early times reduces the accretion rate of DM and hence the total mass of the halo at $z = 0$. This effect lowers the V_{max} of all dwarf haloes and produces a net shift in the VF.

The *maximum* possible reduction in the mass of a halo due to internal (i.e. feedback) processes can be modelled as a reduction at high redshift in the total matter abundance by a factor equal to the baryon fraction, $\Omega_{\mathrm{bar}} \to 0$. The total matter density then becomes

$$\Omega_{\mathrm{m}}^{\mathrm{int}} = \Omega_{\mathrm{m}} - \Omega_{\mathrm{bar}}, \quad (32)$$

where Ω_{m} and Ω_{m} are the *Planck* total matter and baryon densities. Since the power spectrum includes a contribution from baryons, the reduction in the baryon density causes a reduction of the power given by

$$P^{\mathrm{int}}(k) = (\Omega_{\mathrm{m}}^{\mathrm{int}}/\Omega_{\mathrm{m}})^2 P_{\mathrm{DM}}(k) = (\Omega_{\mathrm{DM}}/\Omega_{\mathrm{m}})^2 P(k). \quad (33)$$

Using $\Omega_{\mathrm{m}}^{\mathrm{int}}$ and $P^{\mathrm{int}}(k)$ in the extended Press–Schechter formalism (Schneider, Smith & Reed 2013; Schneider et al. 2014; Schneider 2015) allows us to obtain the new feedback-modified VF. The result can be fitted with a simple reduction of the velocities,

$$V_{\mathrm{max}}^{\mathrm{int}} = f_{\mathrm{int}} V_{\mathrm{max}}, \quad (34)$$

with $f_{\mathrm{int}} = 0.86$. This is equivalent to a ∼40 per cent reduction in the normalization of the VF. The total effect from external UV photoevaporation plus internal feedback baryon depletion on the VF of DM haloes is then

$$\Phi_{\mathrm{gal}}(V_{\mathrm{max}}) = \mathcal{F}_{\mathrm{ext}}(V_{\mathrm{max}}^{\mathrm{int}}/f_{\mathrm{int}}) \times \Phi_{\mathrm{CDM}}(V_{\mathrm{max}}^{\mathrm{int}}/f_{\mathrm{int}}). \quad (35)$$

Fig. 11 shows the new CDM VF corrected for baryonic effects. The abundance of detected DM haloes at the lowest observed V_{max} is about five times lower than the original collisionless CDM estimate. This is, however, not enough to bring it into agreement with the observed galaxy V_{max} function in the LV obtained in Section 4.1. Allowing for the maximum feedback and photoevaporation suppression, at $V_{\mathrm{max}} = 30$ km s^{-1} the CDM galactic VF is still at least a factor of ∼2.5 (with greater than 99.97 per cent confidence) above the observed V_{max} VF regardless of the assumed core/cusp nature of the density profiles. The disagreement between CDM and observations becomes significant for haloes with $V_{\mathrm{max}} < 60$ km s^{-1}, with the theory predicting ∼1.8 times more galaxies than observed at $V_{\mathrm{max}} = 50$ km s^{-1}.

Fig. 11 also shows the V_{max} VF of the APOSTLE simulations derived using the V_{max}–M_{bar} relation from Sales et al. (2017) shown in Fig. 10. Although the V_{max}–M_{bar} of APOSTLE is similar to our maximum suppression model, its smaller scatter around the relation produces a sharper cut-off in the VF (at the completeness limit of the LV).

5 COMPARISON TO OTHER STUDIES

Brook & Shankar (2016) performed an analysis of the rotation measurement biases in the local VF using data from the ALFALFA survey (Haynes et al. 2011). They modified the theoretical CDM VF using abundance matching and then applied various observational BTFRs to obtain the 'observed' ALFALFA $W50$ VF. They find that the definition of rotation velocity fully accounts for the large disagreement between CDM and the observed galaxy VF.

Our conclusions are strikingly different from Brook & Shankar (2016) due to two of their key assumptions. First, the ALFALFA BTFR used by Brook & Shankar (2016) is much shallower than the one we obtained for the LV (equation 2). Secondly, their use of abundance matching guarantees *by construction* that any theoretical halo VF will produce the observed VF. This is simply because the mapping between halo V_{max} and M_{bar} provided by abundance matching is an ingredient of the model itself, and this ensures that the observed galaxy VF will always recover the *input* halo VF that was assumed in deriving it (even if one assumed a non-CDM VF). Hence, an independent verification of the CDM halo VF would be necessary to confirm the conclusions of Brook & Shankar (2016). We have shown in our analysis that spatially resolved dwarf kinematic data do not agree with the CDM halo VF (see Fig. 9).

To understand why the ALFALFA BTFR that Brook & Shankar (2016) utilize is shallower, we repeated our analysis on the

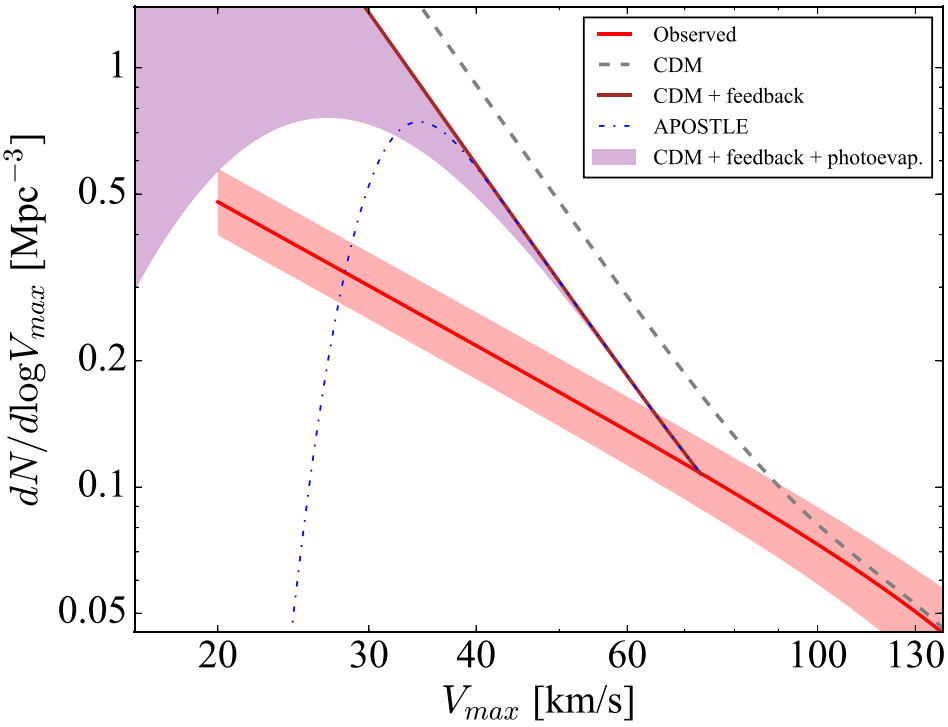

Figure 11. Theoretical CDM VF including the effects of stellar feedback and photoevaporation. The dashed curve is the parametrization of the CDM halo VF from K15. The lower solid curve includes the reduction of circular velocities of haloes due to feedback-powered outflows. The shaded area includes the 3σ allowed region of suppression of halo detection due to photoevaporation from an ionizing background (see Fig. 10). The dot–dashed curve represents the result of using the simulated APOSTLE BTFR from Fig. 10 to correct the theoretical halo VF for baryonic suppression effects.

ALFALFA catalogue. Using these data is more challenging because the survey is magnitude instead of volume limited. This, combined with systematics in the faintest objects, yields a BTFR that is poorly defined at the low-mass end. Forward fits (where $\log M_{\rm bar}$ is the dependent variable) are known to produce a bias towards shallower slopes in Tully–Fisher studies (see e.g. Bradford, Geha & van den Bosch 2016) due to completeness issues at low $M_{\rm bar}$, and to the presence of outliers.

Fig. 12 shows the result of performing an inverse linear fit (where $V50 = W50/2$ is the dependent variable) to the ALFALFA data. To account for deviations from a power law, we also show the binned statistics for 10 equally spaced logarithmic bins in baryon mass. The binned fit to the ALFALFA line-of-sight velocities as a function of $M_{\rm bar}$ is comparable to the fit for the LV BTFR (equation 2). Therefore, using the ALFALFA data set to construct a $V_{\rm max}$ VF of the local Universe using equation (17) would yield the same result as shown in Fig. 7. This indicates that the ALFALFA data are consistent with the LV sample once the systematics are taken into account.

Macciò et al. (2016) used a suite of 87 galaxy formation simulations from the NIHAO project to obtain a correction from 'observed' H I linewidths to the $V_{\rm max}$ of the host DM halo. These simulations explicitly included gas dynamics and metal cooling as well as standard recipes for subgrid physics such as star formation and stellar feedback. When applied to the galaxy VF, their correction is large enough to bring the observations into agreement with the CDM halo VF. To find the origin of the disagreement with our conclusions, we first compare the global properties of the simulations with our data and then directly examine the measurements of rotation velocity in NIHAO and the P16 data.

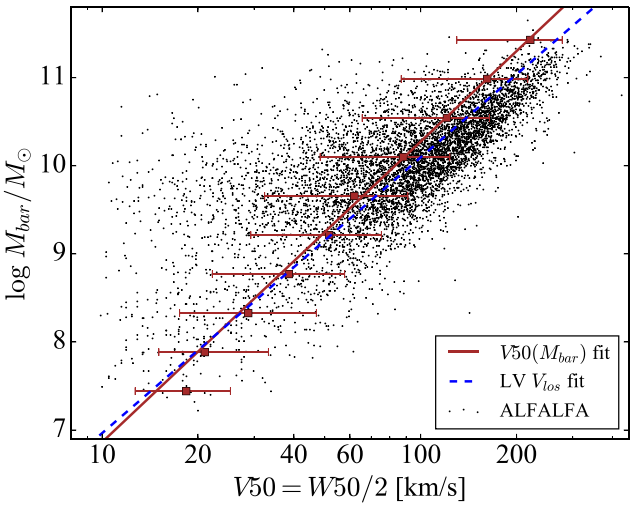

Figure 12. ALFALFA data compared to the LV sample. Points represent the ALFALFA galaxies. The solid line is a linear fit to $\log V50(\log M_{\rm bar})$. Squares with error bars indicate the mean and standard deviation of the data in uniform $\log M_{\rm bar}$ bins. The dashed line reproduces the fit to the LV line-of-sight velocities from Fig. 2. The ALFALFA fit is essentially identical to the LV for $V50 < 60$ km s^{-1}.

Fig. 13 shows a comparison of the $V_{\rm max}$ BTFR of NIHAO with the spatially resolved P16 profile fits. At a fixed baryonic mass, the NIHAO faint dwarfs inhabit haloes with larger $V_{\rm max}$ than observed galaxies. For $M_{\rm bar} < 10^8$ M$_\odot$, the discrepancy between NIHAO and observations can be larger than a factor of $\sim$2 in $V_{\rm max}$ or about a

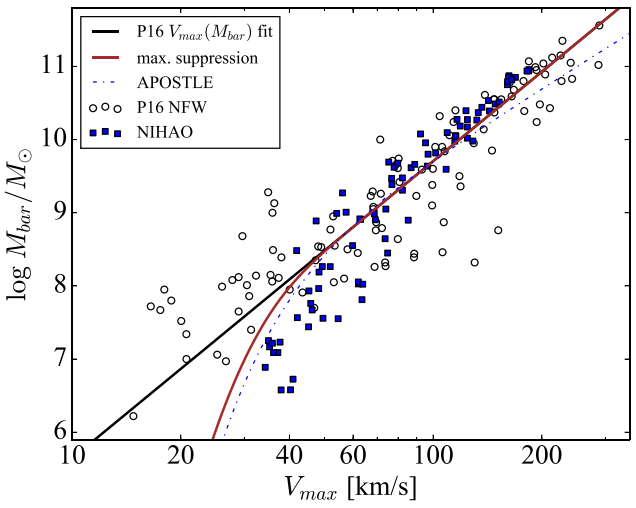

Figure 13. Baryonic mass as a function of halo maximum circular velocity for the P16 selected sample compared to the NIHAO simulations. The APOSTLE and NIHAO simulated galaxies with $V_{\rm max}$ below ∼50 km s^{-1} display a characteristic steep downturn in the relation that allows them to reproduce the theoretical CDM VF.

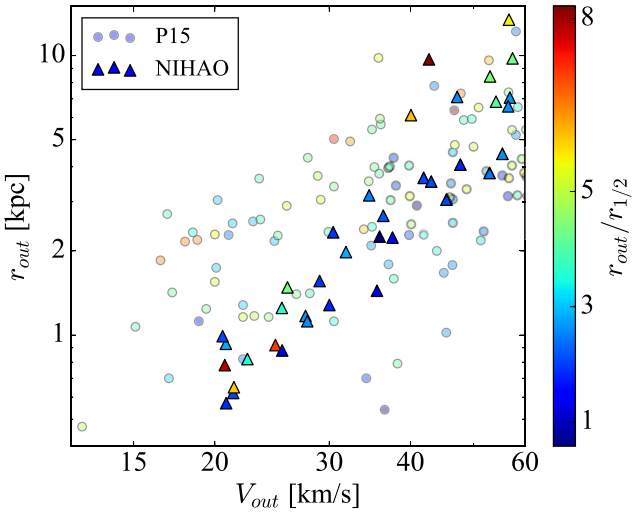

Figure 14. Outermost kinematic radius versus $V_{\rm out}$ for the simulated NIHAO galaxies compared to the low-mass P16 observed galaxies. The colour bar shows the relative extent of the H I disc with respect to the half-light radius. For NIHAO, $V_{\rm out}$ is the circular velocity at the radius enclosing 90 per cent of the H I mass, and the projected half-light radius is measured using mock V-band observations. On average, observed dwarfs with $V_{\rm rot} < 40\,{\rm km\,s^{-1}}$ have significantly more extended H I kinematic radii than the simulations. The NIHAO objects in this range typically have smaller discs than their observed counterparts.

factor of 10 in halo mass. This difference is due to a sharp downturn in the baryonic mass of the NIHAO dwarfs below ∼50 km s^{-1}, which is not present in the data. This steeper BTF allows the simulations to reproduce the theoretical CDM VF.

Macciò et al. (2016) argue that compared to massive galaxies, the thicker and highly turbulent H I discs of dwarfs lead to observed H I profile widths that fail to trace the gravitational potential of the halo, resulting in an underestimation of $V_{\rm max}$. Our method relies on resolved kinematic measurements that take into account turbulent support to obtain $V_{\rm out}$. This should make $V_{\rm out}$ a better tracer of the potential than the linewidth. None the less, the results of our analysis would not hold if it could be demonstrated that pressure-corrected gas rotation curves are in general a poor tracer of the mass distribution in dwarf galaxies. If this is the case in the NIHAO simulated dwarfs, it could explain the disagreement.

Given that comparisons of the simulations with properties inferred indirectly from observations such as $V_{\rm max}$ are prone to observational systematics (as discussed above), we may instead compare direct observables. We find the following differences.

First, at a fixed $V_{\rm out}$, the simulations typically show smaller deprojected linewidths than observations. In a detailed analysis, Papastergis & Ponomareva (2017) compared the full circular velocity profiles of the lowest mass NIHAO hydrodynamic runs to the outermost rotation measurement of the P16 dwarfs with comparable H I 50 per cent linewidths. They find that dwarf galaxies with large kinematic radii ($r_{\rm out} > 1.5$ kpc) have $V_{\rm out}$ significantly below the circular velocity of the NIHAO counterparts, and conclude that these objects cannot be explained by the simulations. They also find that dwarf galaxies with large kinematic radii have, on average, larger $V_{\rm rot}$ than the NIHAO counterparts. Fig. E1 shows that the linewidth-derived $V_{\rm rot}$ traces, on average, the outermost rotation velocity $V_{\rm out}$ of the P16 sample to within ∼10 per cent with an rms scatter of ∼20 per cent.

Secondly, the cold gas discs of the low-mass NIHAO simulations may be less extended than observed dwarfs. In Fig. 14, we show the kinematic extent of the P16 and NIHAO dwarfs as a function of their outermost H I rotation velocity. In both cases, $r_{\rm out}$ is near the edge of the H I disc.[9] For objects with $V_{\rm out} \gtrsim 40\,{\rm km\,s^{-1}}$, the extent of the simulated discs seems to match the data. However, at lower velocities, the simulations appear to have, on average, systematically smaller H I discs than observed dwarfs. This may be a consequence of the UV background assumed in the simulations. Smaller simulated discs could contribute partly to the disagreement with our VF results at $V_{\rm out} \lesssim 40\,{\rm km\,s^{-1}}$. As shown in Fig. 5, for a galaxy with a given measured $V_{\rm out}$, the smaller $r_{\rm out}$ of NIHAO requires fitting with a more massive DM halo and a larger $V_{\rm max}$. This, in turn, would increase the size of the correction between $V_{\rm rot}$ and $V_{\rm max}$ shown in Fig. 6. Moreover, the formation of shallow DM cores in NIHAO (Tollet et al. 2016) allows for even larger haloes to be fit when $r_{\rm out} \lesssim r_{\rm core}$. It is important to note, however, that this comparison is not definitive as it is based on the radii that enclose 90 per cent of the H I mass in the simulations, whereas observers typically define the edge of the disc at a gas surface density of 1 M$_\odot$ pc^{-2}.

Summarizing, our overall disagreement with the Macciò et al. (2016) results likely originates from a combination of highly turbulent simulated gas discs that reduce the H I linewidths at fixed $V_{\rm out}$ and $V_{\rm max}$ in the simulations, and possibly smaller-than-observed H I simulated discs in faint dwarfs. The most direct diagnostic, avoiding biases in derived quantities such as $V_{\rm max}$, is the relation between $W50$ and $V_{\rm out}$. The H I linewidths of the NIHAO dwarf simulations are typically lower at a fixed value of $V_{\rm out}$. As noted by Papastergis & Ponomareva (2017), a selection bias towards extended rotating neutral gas discs in the P16 data might explain the disagreement. In addition, it is also possible that the discrepancy results from the failure of pressure-corrected rotation curves to accurately recover

[9] However, in the NIHAO simulations, $r_{\rm out}$ is defined as the radius enclosing 90 per cent of the H I mass.

the circular velocity (e.g. due to disequilibrium or radial motions). To examine this possibility would require mock observations of the simulated galaxies and is beyond the scope of this work. Note, however, that Read et al. (2016b) use high-resolution simulations to argue against this scenario. Lastly, another effect that might increase the discrepancy in Fig. 14 is a systematic difference in the way the extent of the H I disc is estimated. More detailed comparisons with the simulations are necessary to rule out this possibility.

6 CONCLUSIONS

In this paper, we have performed a detailed analysis of galaxies in the LV to obtain the VF of the DM haloes that host the faintest known dwarfs. We have shown that the tightly correlated BTFR can be used to correct, on average, the systematic underestimation of the maximum circular velocity in kinematic data derived from spatially unresolved H I linewidths. Employing the largest available sample of dwarf galaxy spatially resolved kinematic data together with the LV catalogue, we obtained a *statistical* relation to connect the linewidth-derived $V_{\rm rot}$ to the average halo $V_{\rm max}$ as a function of $M_{\rm bar}$ by way of using parametrized mass models. This relation allowed us to derive a $V_{\rm max}$ VF of galaxies for unmodified NFW as well as feedback-induced cored DM density profiles. The observed $V_{\rm max}$ VF of galaxies in the LV was compared to theoretical and observational estimates of the effect of photoevaporation and stellar feedback on the theoretical CDM halo VF. Our conclusions are the following.

(i) The observed $V_{\rm max}$ VF of galaxies is slightly steeper than the line-of-sight VF and has a higher normalization (due mainly to inclination effects). The slightly steeper slope is a result of the $V_{\rm max}$–$V_{\rm rot}$ relation (Fig. 6). The new $V_{\rm max}$ VF is still well below the theoretical CDM halo VF for scales below $V_{\rm max} \sim 80$ km s^{-1} (Fig. 7).

(ii) Feedback-induced DM cores do not significantly affect the observed $V_{\rm max}$ VF. This occurs because a large fraction of kinematic measurements extend well outside the region where cores are expected to form (within ∼2 half-light radii), producing fits with the same halo mass (and hence $V_{\rm max}$) as in the case with unmodified NFW profiles (Fig. 9).

(iii) The maximum effect of stellar feedback on the CDM halo abundance can be estimated using a reduction of the cosmic baryon density and power spectrum amplitude at high redshift. The net effect is a reduction of the normalization of the VF of ∼40 per cent (Fig. 11).

(iv) Photoevaporation of gas due to reionization can be modelled as bend in the power-law relation between baryonic mass and halo $V_{\rm max}$ (Fig. 10). The break is not detected in current data but we can obtain an allowed (3σ) limit on the reduction of halo detection due to reionization suppression (Fig. 10). The data suggest that the impact of photoevaporation from ionizing radiation could become important for galaxies with $V_{\rm max} \lesssim 40$ km s^{-1}. The theoretical CDM dwarf galaxy abundance is reduced by up to a factor of ∼2 for haloes with $V_{\rm max} \approx 30$ km s^{-1} (Fig. 11).

(v) The theoretical CDM VF with maximum baryonic suppression is still ∼1.8 times higher (at the 3σ level) than the observed $V_{\rm max}$ VF at $V_{\rm max} = 50$ km s^{-1}, and a factor of ∼2.5 higher at $V_{\rm max} = 30$ km s^{-1} in the LV. The discrepancy is likely to be larger if the baryonic effects are not maximal as we assumed. This discrepancy could point to the necessity of a modification of the cosmological predictions on small scales. Possible alternatives are provided by warm or self-interacting DM models.

(vi) We can compare our results to state-of-the-art galaxy formation simulations that claim to reduce the discrepancy between the observed VF and CDM. Assuming that pressure-corrected rotation curves trace, on average, the circular velocity, the disagreement results from three effects in the simulations: a steep downturn in the $V_{\rm max}$ BTFR at $M_{\rm bar} \lesssim 10^8$ M$_\odot$ (Fig. 13), a reduction in the H I extent of the lowest mass dwarfs, and an underestimation of the linewidth compared to the outermost rotation velocity in the kinematically hot simulated H I discs. The BTF downturn is disfavoured by the data (Fig. 10), while observations suggest that the mean linewidth-derived rotation velocity deviates from $V_{\rm out}$ by less than ∼10 per cent (Fig. E1), and that simulated H I discs may be too small (Fig. 14).

Finally, we would like to note that our analysis rests on the assumption that our compiled sample of resolved kinematic data is representative of the galaxy population, and not biased towards galaxies with extended and rotationally supported H I discs. Our method also relies on the customary assumption that extended H I rotation curve measurements (including turbulence corrections) are a good probe of the gravitational potential of the DM halo hosting the galaxy. If this assumption was shown to be invalid at dwarf galaxy scales, our conclusions may no longer hold. While it is extremely difficult to test the validity or accuracy of the asymmetric drift correction in dwarfs, Read et al. (2016b) recently showed that in simulated galaxies with dispersions similar to observed dwarfs, the standard pressure support-corrected rotation curves yield accurate estimates of $V_{\rm circ}$. In a future paper, we will further explore this issue using hydrodynamical simulations.

In the next paper in this series (Schneider et al. 2017), we explore the VFs predicted by alternative DM models, including baryonic effects, and compare them to the observed $V_{\rm max}$ VF obtained using the methods described here.

ACKNOWLEDGEMENTS

We would like to thank the anonymous referee for suggesting revisions that greatly improved the quality of the paper. We also thank Anatoly Klypin for insightful discussions, and Andrea Macciò and Aaron Dutton for generously providing their NIHAO data. AS acknowledges support from the Swiss National Science Foundation (PZ00P2_161363).

REFERENCES

Arraki K. S., Klypin A., More S., Trujillo-Gomez S., 2014, MNRAS, 438, 1466
Bekeraitė S. et al., 2016, ApJ, 827, L36
Boylan-Kolchin M., Bullock J. S., Kaplinghat M., 2011, MNRAS, 415, L40
Bradford J. D., Geha M. C., Blanton M. R., 2015, ApJ, 809, 146
Bradford J. D., Geha M. C., van den Bosch F. C., 2016, ApJ, 832, 11
Brook C. B., Shankar F., 2016, MNRAS, 455, 3841
Brook C. B. et al., 2011, MNRAS, 415, 1051
Brook C. B., Stinson G., Gibson B. K., Wadsley J., Quinn T., 2012, MNRAS, 424, 1275
Brooks A. M., Zolotov A., 2014, ApJ, 786, 87
Brooks A. M., Kuhlen M., Zolotov A., Hooper D., 2013, ApJ, 765, 22
Di Cintio A., Brook C. B., Dutton A. A., Macciò A. V., Stinson G. S., Knebe A., 2014, MNRAS, 441, 2986 (DC14)
Diemand J., Kuhlen M., Madau P., 2007, ApJ, 667, 859
Dutton A. A., Macciò A. V., 2014, MNRAS, 441, 3359
Gnedin N. Y., 2000, ApJ, 542, 535
Governato F. et al., 2010, Nature, 463, 203

Governato F. et al., 2012, MNRAS, 422, 1231
Haynes M. P. et al., 2011, AJ, 142, 170
Heitmann K. et al., 2016, ApJ, 820, 108
Hellwing W. A., Frenk C. S., Cautun M., Bose S., Helly J., Jenkins A., Sawala T., Cytowski M., 2016, MNRAS, 457, 3492
Hoeft M., Yepes G., Gottlöber S., Springel V., 2006, MNRAS, 371, 401
Iorio G., Fraternali F., Nipoti C., Di Teodoro E., Read J. I., Battaglia G., 2017, MNRAS, 466, 4159
Jarrett T. H., Chester T., Cutri R., Schneider S. E., Huchra J. P., 2003, AJ, 125, 525
Karachentsev I. D., Makarov D. I., Kaisina E. I., 2013, AJ, 145, 101
Klypin A., Kravtsov A. V., Valenzuela O., Prada F., 1999, ApJ, 522, 82
Klypin A. A., Trujillo-Gomez S., Primack J., 2011, ApJ, 740, 102
Klypin A., Karachentsev I., Makarov D., Nasonova O., 2015, MNRAS, 454, 1798 (K15)
Lelli F., Verheijen M., Fraternali F., 2014, A&A, 566, A71
Lelli F., McGaugh S. S., Schombert J. M., 2016, AJ, 152, 157
Macciò A. V., Udrescu S. M., Dutton A. A., Obreja A., Wang L., Stinson G. R., Kang X., 2016, MNRAS, 463, L69
McGaugh S. S., 2012, AJ, 143, 40
Mashchenko S., Wadsley J., Couchman H. M. P., 2008, Science, 319, 174
Moore B., Ghigna S., Governato F., Lake G., Quinn T., Stadel J., Tozzi P., 1999, ApJ, 524, L19
Munshi F. et al., 2013, ApJ, 766, 56
Nagashima M., Okamoto T., 2006, ApJ, 643, 863
Navarro J. F., Frenk C. S., White S. D. M., 1997, ApJ, 490, 493
Oh S.-H., de Blok W. J. G., Brinks E., Walter F., Kennicutt R. C., Jr, 2011, AJ, 141, 193
Oh S.-H. et al., 2015, AJ, 149, 180
Okamoto T., Gao L., Theuns T., 2008, MNRAS, 390, 920
Oñorbe J., Boylan-Kolchin M., Bullock J. S., Hopkins P. F., Kereš D., Faucher-Giguère C.-A., Quataert E., Murray N., 2015, MNRAS, 454, 2092
Papastergis E., Shankar F., 2016, A&A, 591, A58
Papastergis E., Ponomareva A. A., 2017, A&A, 601, A1
Papastergis E., Martin A. M., Giovanelli R., Haynes M. P., 2011, ApJ, 739, 38
Papastergis E., Giovanelli R., Haynes M. P., Shankar F., 2015, A&A, 574, A113
Papastergis E., Adams E. A. K., van der Hulst J. M., 2016, A&A, 593, A39
Pontzen A., Governato F., 2012, MNRAS, 421, 3464
Read J. I., Agertz O., Collins M. L. M., 2016a, MNRAS, 459, 2573
Read J. I., Iorio G., Agertz O., Fraternali F., 2016b, MNRAS, 462, 3628
Reed D. S., Smith R. E., Potter D., Schneider A., Stadel J., Moore B., 2013, MNRAS, 431, 1866
Sales L. V. et al., 2017, MNRAS, 464, 2419
Sawala T. et al., 2015, MNRAS, 448, 2941
Sawala T. et al., 2016, MNRAS, 457, 1931
Schneider A., 2015, MNRAS, 451, 3117
Schneider A., Smith R. E., Reed D., 2013, MNRAS, 433, 1573
Schneider A., Anderhalden D., Macciò A. V., Diemand J., 2014, MNRAS, 441, L6
Schneider A., Trujillo-Gomez S., Papastergis E., Reed D. S., Lake G., 2017, MNRAS, 470, 1542
Shen S., Madau P., Conroy C., Governato F., Mayer L., 2014, ApJ, 792, 99
Somerville R. S., 2002, ApJ, 572, L23
Springel V. et al., 2005, Nature, 435, 629
Stilp A. M., Dalcanton J. J., Warren S. R., Skillman E., Ott J., Koribalski B., 2013, ApJ, 765, 136
Swaters R. A., Sancisi R., van Albada T. S., van der Hulst J. M., 2009, A&A, 493, 871
Teyssier R., Pontzen A., Dubois Y., Read J. I., 2013, MNRAS, 429, 3068
Tikhonov A. V., Klypin A., 2009, MNRAS, 395, 1915
Tollet E. et al., 2016, MNRAS, 456, 3542
Trujillo-Gomez S., Klypin A., Primack J., Romanowsky A. J., 2011, ApJ, 742, 16
Trujillo-Gomez S., Klypin A., Colín P., Ceverino D., Arraki K. S., Primack J., 2015, MNRAS, 446, 1140
Wang L., Dutton A. A., Stinson G. S., Macciò A. V., Penzo C., Kang X., Keller B. W., Wadsley J., 2015, MNRAS, 454, 83
Warren S. R. et al., 2012, ApJ, 757, 84
Wheeler C., Oñorbe J., Bullock J. S., Boylan-Kolchin M., Elbert O. D., Garrison-Kimmel S., Hopkins P. F., Kereš D., 2015, MNRAS, 453, 1305
Zavala J., Jing Y. P., Faltenbacher A., Yepes G., Hoffman Y., Gottlöber S., Catinella B., 2009, ApJ, 700, 1779
Zolotov A. et al., 2012, ApJ, 761, 71
Zwaan M. A., Meyer M. J., Staveley-Smith L., 2010, MNRAS, 403, 1969

APPENDIX A: INCLINATION UNCERTAINTIES

Fig. A1 shows the BTFRs of the high-inclination ($i > 60$) LV and P16 subsamples. The inclination uncertainty in these objects is minimized compared to the full samples. Both the high-inclination LV and P16 dwarf galaxies have significantly lower rotation velocities than the full samples. As discussed by Papastergis & Shankar (2016), this arises because the stellar discs of dwarf galaxies are thicker than those of bright spirals. For low-inclination dwarfs, the assumption of infinitely thin discs can lead to underestimated inclinations, resulting in an overestimate of the deprojected rotation velocity.

To avoid this systematic effect in our analysis, we used the line-of-sight rotation velocity of the LV galaxies. In addition, as discussed in Section 3.2, removing the inclination errors in the P16 sample would reduce the average $V_{\rm out}$ at a fixed $M_{\rm bar}$, allowing for lower mass haloes to be fitted to the same galaxies. This would have the overall effect of a systematic shift in the observed $V_{\rm max}$ VF towards smaller circular velocities, making the disagreement with CDM predictions even worse.

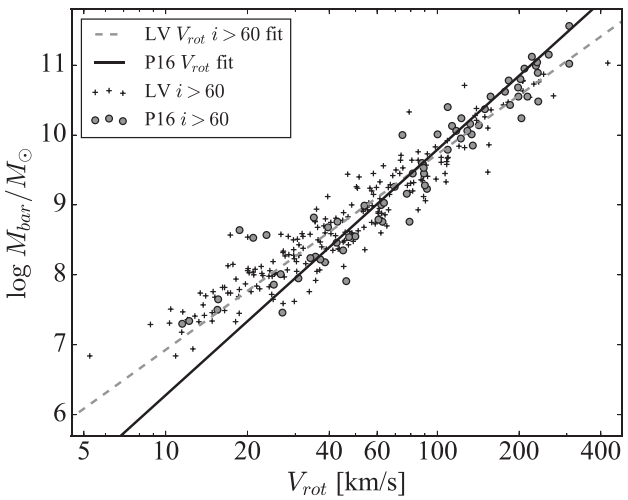

Figure A1. BTFR of the high-inclination objects from the LV and P16 samples. The solid circles show the P16 galaxies, while the crosses represent the LV galaxies. The solid line is the fit to the full P16 sample from equation (3), while the dashed line is a linear fit to the high-inclination LV objects.

APPENDIX B: NON-PARAMETRIC DESCRIPTION OF THE BTFR DATA

Fig. B1 shows a comparison of the linear regressions used to describe the BTF data in Section 3.2 with the distribution of the deprojected linewidths of the LV and P16 data in uniform $\log M_{\rm bar}$ bins. The power-law fits used in our analysis appropriately capture the relation between baryonic mass and line-of-sight velocity in

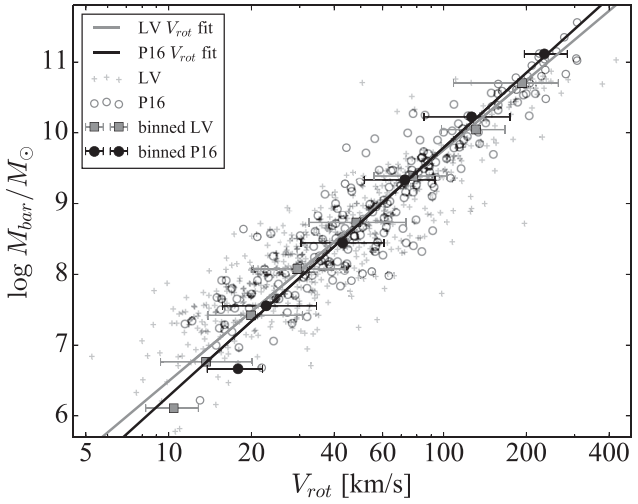

Figure B1. Non-parametric description of the BTFRs of the LV and P16 data using the deprojected H I linewidth. The symbols with error bars represent the sample mean and standard deviation in uniform log $M_{\rm bar}$ bins. The lines reproduce the fits shown in Fig. 3. The power-law fits used in our analysis are an excellent representation of the non-parametric binned data except in the lowest mass bins where data are scarce.

both samples and no extra degrees of freedom are necessary in the fits.

APPENDIX C: SENSITIVITY OF THE RESULTS TO SAMPLE SELECTION

Fig. C1 shows the sensitivity of the linear fit from equation (16) to changes in the minimum value of the relative kinematic extent, $r_{\rm out}/r_{1/2}$, allowed in the P16 sample selection. The figure shows the slope and intercept of the fit obtained from binning the error-weighted $V_{\rm max}$ values as was done in Fig. 6.

The observed variation in the fit parameters is relatively small and the largest deviations in the slope are compensated by changes in the intercept, which result in a fit that is largely insensitive to the data selection.

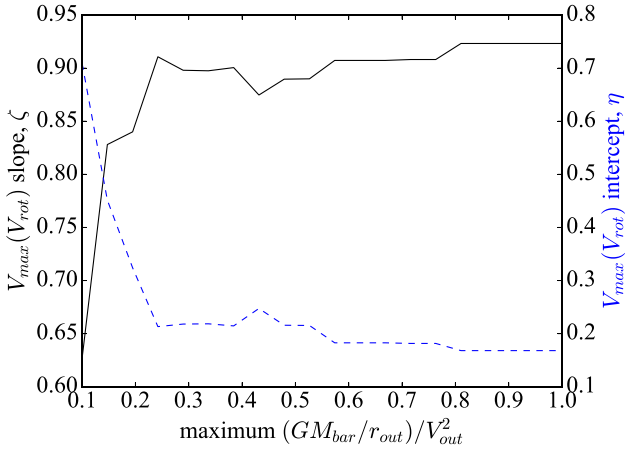

Figure C2. Effect of varying the maximum allowed contribution from the baryonic mass to the circular velocity. The left axis and solid line correspond to the slope, ζ, and the right axis and dashed line show the intercept, η. Only cuts that preserve more than 60 data points are shown.

To check the robustness of the second sample cut, we plot in Fig. C2 the variation of the same parameters when the maximum allowed contribution from baryons to the circular velocity, $(GM_{\rm bar}/r_{\rm out})/V^2_{\rm out}$, is varied.

Although the slope and intercept vary considerably for values $(GM_{\rm bar}/r_{\rm out})/V^2_{\rm out} < 0.2$, the intercept increases while the slope decreases to produce a relatively small net change in the predictions of the model.

APPENDIX D: COMPARISON WITH OTHER PARAMETRIZATIONS OF CORED HALO PROFILES

The Di Cintio et al. (2014, hereafter DC14) parametrization of the DM density profile of galaxies including feedback-induced cores has been extensively used in the literature. In this work, we used instead the fit by Read et al. (2016a, the 'coreNFW' profile) to evaluate the effect of DM cores on the observed $V_{\rm max}$ VF. Fig. D1

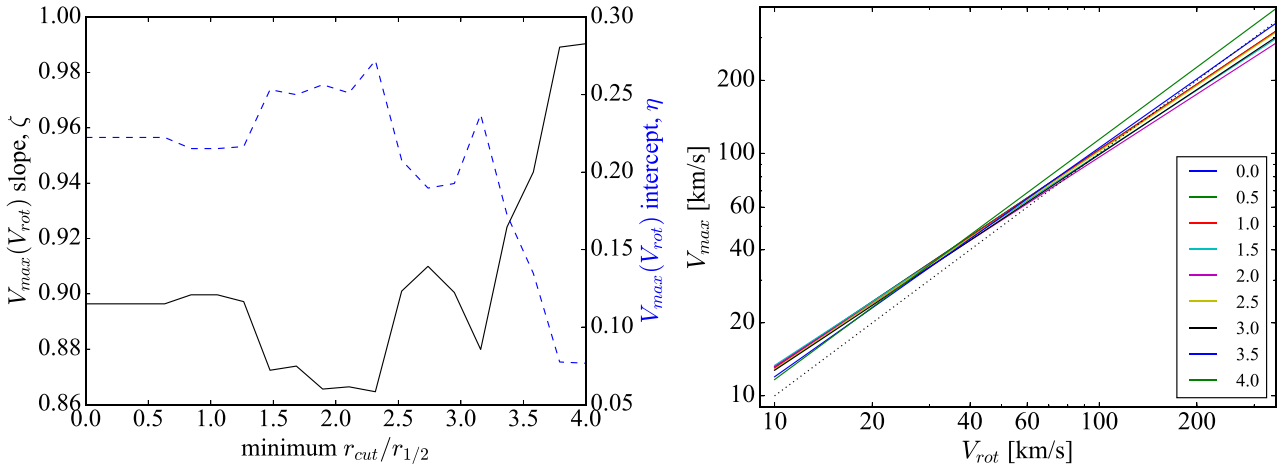

Figure C1. Effect of varying the minimum $r_{\rm out}/r_{1/2}$ of the P16 sample on the linear fit to equation (16). Left: the left axis and solid line correspond to the slope, ζ, and the right axis and dashed line show the intercept, η. Right: comparison of the models. The value of $r_{\rm out}/r_{1/2}$ for each model is indicated in the legend. The dotted line shows $V_{\rm max} = V_{\rm rot}$. Only cuts that preserve more than 60 data points are shown. The variation in the fit parameters is relatively small, with the slope changes usually compensated by changes in the intercept to produce a robust fit at low velocities.

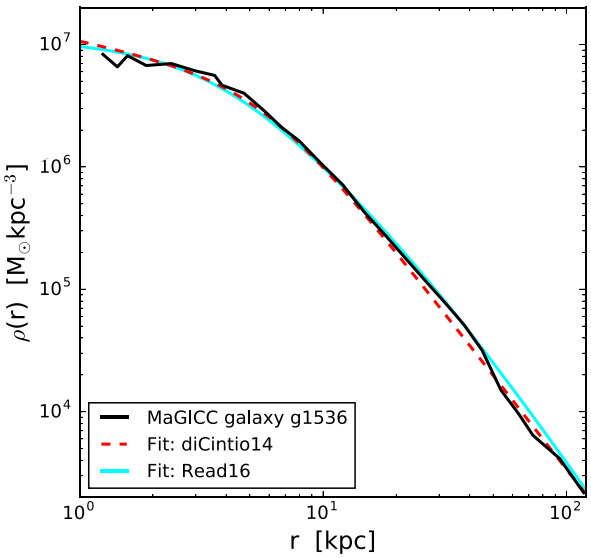

Figure D1. Comparison of the DC14 and Read et al. (2016a) cored DM halo profile parametrizations. The solid black line is the density profile of the hydrodynamical galaxy simulation g1536 from DC14. The dashed and solid curves are the DC14 and coreNFW fits, respectively.

shows a comparison of the two fits applied to a simulation from the MAGICC suite (DC14). Since the DC14 fit depends critically on the ratio $M_{\rm star}/M_{\rm vir}$, we used the values reported for the simulation by DC14. For the coreNFW fit, we took the half-light radius of the same simulation from Brook et al. (2012), assumed a flat core with $n = 1$, and varied the concentration to obtain a good fit. The figure shows that the coreNFW fit is also a good description of the DM core formed in the simulation.

This example further confirms the validity of the coreNFW profile for accurately capturing the extent of feedback-induced cores in hydrodynamic simulations. Our results are therefore independent of our choice of cored profile model.

APPENDIX E: HOW ACCURATELY DOES THE LINEWIDTH-DERIVED $V_{\rm rot}$ TRACE $V_{\rm out}$?

Fig. E1 shows the ratio between $V_{\rm rot}$ and $V_{\rm out}$ for the P16 observations. The average linewidth-derived rotation velocity traces the outermost rotation velocity of the galaxies to within ∼10 per cent.

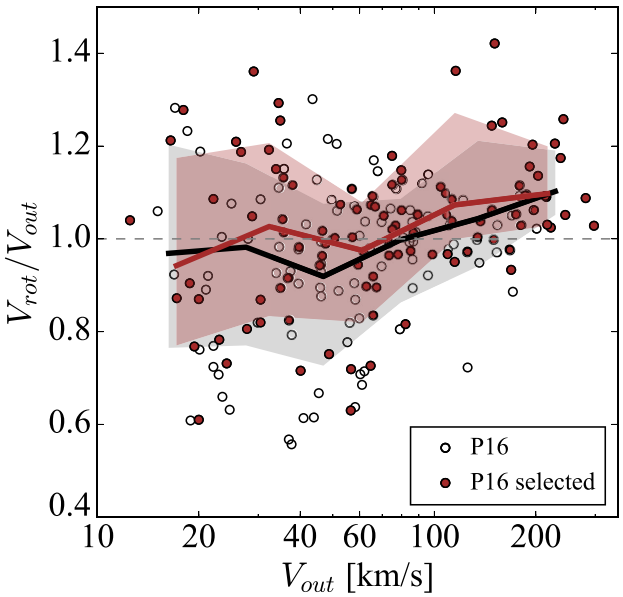

Figure E1. Ratio between the deprojected line-of-sight velocity $V_{\rm rot}$ and the outermost rotation measurement $V_{\rm out}$ for the galaxies in the P16 sample. The open symbols show the full sample while filled symbols show the selected subsample with $r_{\rm out} > 3r_{1/2}$. The solid lines and shading represent the means and rms scatter in uniform log $V_{\rm out}$ bins.

This paper has been typeset from a TEX/LATEX file prepared by the author.